

A MICROMECHANICS BASED DUCTILE DAMAGE MODEL FOR
ANISOTROPIC TITANIUM ALLOYS

A Thesis

by

SHYAM MOHAN KERALAVARMA

Submitted to the Office of Graduate Studies of
Texas A&M University
in partial fulfillment of the requirements for the degree of

MASTER OF SCIENCE

May 2008

Major Subject: Aerospace Engineering

A MICROMECHANICS BASED DUCTILE DAMAGE MODEL FOR
ANISOTROPIC TITANIUM ALLOYS

A Thesis

by

SHYAM MOHAN KERALAVARMA

Submitted to the Office of Graduate Studies of
Texas A&M University
in partial fulfillment of the requirements for the degree of

MASTER OF SCIENCE

Approved by:

Chair of Committee,	Amine Benzerga
Committee Members,	Dimitris Lagoudas
	Xin-Lin Gao
Head of Department,	Helen Reed

May 2008

Major Subject: Aerospace Engineering

ABSTRACT

A Micromechanics Based Ductile Damage Model for Anisotropic Titanium Alloys.

(May 2008)

Shyam Mohan Keralavarma, B.Tech, University of Kerala, India

Chair of Advisory Committee: Dr. Amine Benzerga

The hot-workability of Titanium (Ti) alloys is of current interest to the aerospace industry due to its widespread application in the design of strong and light-weight aircraft structural components and engine parts. Motivated by the need for accurate simulation of large scale plastic deformation in metals that exhibit macroscopic plastic anisotropy, such as Ti, a constitutive model is developed for anisotropic materials undergoing plastic deformation coupled with ductile damage in the form of internal cavitation. The model is developed from a rigorous micromechanical basis, following well-known previous works in the field. The model incorporates the porosity and void aspect ratio as internal damage variables, and seeks to provide a more accurate prediction of damage growth compared to previous existing models. A closed form expression for the macroscopic yield locus is derived using a Hill-Mandel homogenization and limit analysis of a porous representative volume element. Analytical expressions are also developed for the evolution of the internal variables, porosity and void shape. The developed yield criterion is validated by comparison to numerically determined yield loci for specific anisotropic materials, using a numerical limit analysis technique developed herein. The evolution laws for the internal variables are validated by comparison with direct finite element simulations of porous unit cells. Comparison with previously published results in the literature indicates that the new model yields better agreement with the numerically determined yield loci for a wide range of loading paths. Use of the new model in continuum finite element simula-

tions of ductile fracture may be expected to lead to improved predictions for damage evolution and fracture modes in plastically anisotropic materials.

To All My Teachers

ACKNOWLEDGMENTS

I would like to express my sincere gratitude to Dr. Amine Benzerga for his constant encouragement, guidance and financial support without which this work would not have been possible. The time he spent with me, especially at the beginning stages of this work, has been invaluable in enabling me to carry this work to completion.

I would like to thank my committee members Dr. Dimitris Lagoudas and Dr. Xin-Lin Gao for taking time out of their busy schedules to serve on my thesis committee. I also thank the support staff at the Department of Aerospace Engineering for their invaluable assistance at various stages. Last, but not least, I wish to express my love and gratitude to my family and all my friends for their moral support and encouragement at all times.

TABLE OF CONTENTS

CHAPTER		Page
I	INTRODUCTION	1
II	HOMOGENIZATION AND LIMIT ANALYSIS	8
	A. Hill-Mandel Homogenization Theory	9
	B. Limit Analysis of the Macroscopic Yield Criterion	11
III	APPROXIMATE ANALYTICAL YIELD CRITERION FOR ANISOTROPIC POROUS MEDIA	15
	A. Geometry and Coordinates	16
	B. Incompressible Axisymmetric Velocity Fields of Lee and Mear	18
	C. Derivation of the Approximate Analytical Criterion	20
	1. Boundary Conditions	20
	2. Choice of Velocity Fields	22
	3. Derivation of the Yield Criterion	23
	4. Determination of the Criterion Parameters	31
	a. Parameters κ and α_2	31
	b. Parameters C and η	37
	5. Special Cases	39
IV	NUMERICAL DETERMINATION OF THE EXACT YIELD CRITERION	42
	A. Numerical Minimization of the Plastic Dissipation	44
	B. Comparison of the Analytical and Numerical Yield Loci	47
V	EVOLUTION LAWS FOR POROSITY AND VOID SHAPE PARAMETER	59
	A. Evolution of Porosity	59
	B. Evolution of the Shape Parameter	61
	C. Comparison to Finite Element Simulations on Unit Cells	65
VI	DISCUSSION AND CONCLUSIONS	74
	A. Generalizations	74

CHAPTER	Page
B. Conclusions	76
C. Future Work	77
REFERENCES	78
APPENDIX A	83
VITA	87

LIST OF TABLES

TABLE		Page
1	Table of material anisotropy parameters used in the numerical computations.	49
2	Table of material anisotropy parameters from the literature. Adapted from [1].	85

LIST OF FIGURES

FIGURE	Page
1	Wedge crack formed at a grain boundary triple point during hot working of an α Ti-6Al-2Sn-4Zr-2Mo alloy. Micrograph from Semiatin et al. [2]. 2
2	Sketch of a porous representative volume element. 9
3	Porous RVEs considered (a) prolate (b) oblate. 16
4	Base vectors of the spheroidal curvilinear coordinate system (a) prolate (b) oblate. 17
5	Variation of P/x^2 as a function of the eccentricity of the current spheroid e for an isotropic matrix (symbol +), Material 1 (symbol \times) and Material 2 (symbol $*$) from Table 1. In all cases B_{20} and B_{21} were taken as zero. 28
6	Variation of Q/x as a function of the eccentricity of the current spheroid e . In all cases B_{20} and B_{21} were taken as zero. 29
7	Variation of α_2 as a function of e_2 for (a) prolate and (b) oblate RVEs, with $f = 0.01$. Discrete points correspond to numerically determined values of α_2 for isotropic matrix ($*$), Material 1 (+) and Material 2 (\times) from Table 1. 34
8	Variation of $F(e)$ as a function of e for prolate RVEs, with $f = 0.001$ and $w_1 = 5$ (a) Isotropic matrix (b) Material 1 from Table 1. 35
9	Variation of $F(u)$ as a function of u for oblate RVEs, with $f = 0.001$ and $w_1 = 1/5$ (a) Isotropic matrix (b) Material 1 from Table 1. 36
10	(a) Variation of κ with h_t for $h = h_a = 1.0$. (b) Variation of κ with h_a for $h = h_t = 1.0$. In both cases, $f = 0.01$ and $w = 5$ (prolate) and $1/5$ (oblate). 37

FIGURE	Page
11	Comparison of the analytical and numerical yield loci for prolate cavities. (a) Isotropic matrix (b) Material 1 (c) Material 2 (d) Material 3 and porosity, $f = 0.001$ (*), $f = 0.01$ (\times), $f = 0.1$ (+). In all cases, $w_1 = 5$. The solid lines correspond to the analytical criterion of this thesis and the dotted line is from [3]. 50
12	Comparison of the analytical and numerical yield loci for Isotropic matrix (\times), Material 1 (+), Material 2 (*) and Material 3 (\circ), for the case $f = 0.001$ and $w_1 = 5$. The solid lines correspond to the analytical criterion of this thesis and the dotted line is from [3]. 51
13	Comparison of the analytical and numerical yield loci for oblate cavities. (a) Isotropic matrix (b) Material 1 (c) Material 2 (d) Material 3 and porosity, $f = 0.001$ (*), $f = 0.01$ (\times), $f = 0.1$ (+). In all cases, $w_1 = 1/5$. The solid lines correspond to the analytical criterion of this thesis and the dotted line is from [3]. 53
14	Comparison of the analytical and numerical yield loci for Isotropic matrix (\times), Material 1 (+), Material 2 (*) and Material 3 (\circ), and $f = 0.001$, for the case $f = 0.001$ and $w_1 = 1/5$. The solid lines correspond to the analytical criterion of this thesis and the dotted line is from [3]. 54
15	Variation of the yield point under hydrostatic loading, Σ_m^y , as a function of the void aspect ratio, w_1 , for porosity $f = 0.001$, and (a) Isotropic matrix (b) Material 1 (c) Material 2 (d) Material 3. The discrete points are the numerically determined yield points, the solid line correspond to the analytical criterion of this thesis and the dotted line is from [3]. 55
16	Variation of the yield point under hydrostatic loading, Σ_m^y , as a function of the parameter h_t , for $h_a = 1$, $f = 0.001$ and (a) $w_1 = 5$ (b) $w_1 = 2$ (c) $w_1 = 0.5$ (d) $w_1 = 0.2$. The discrete points are the numerically determined yield points, the solid line correspond to the analytical criterion of this thesis and the dotted line is from [3]. 57

FIGURE	Page	
17	Variation of the yield point under hydrostatic loading, Σ_m^y , as a function of the parameter h_a , for $h_t = 1$, $f = 0.001$ and (a) $w_1 = 5$ (b) $w_1 = 2$ (c) $w_1 = 0.5$ (d) $w_1 = 0.2$. The discrete points are the numerically determined yield points, the solid line correspond to the analytical criterion of this thesis and the dotted line is from [3].	58
18	D_m/D_m^{sph} as a function of the void aspect ratio, (a) a_1/b_1 for prolate cavities (b) b_1/a_1 for oblate cavities, stress triaxiality, $T = 1$ and $f = 0.01$. The solid line corresponds to the predictions from the present model, and the dotted line corresponds to the model in [3]. Discrete points correspond to numerically determined values for an isotropic matrix (*), material 1 (+) and material 2 (\times) from Table 1.	62
19	The factor s_h as a function of h_t . The continuous line corresponds to equation (5.16) and the discrete points correspond to numerically determined values for various values of h_a . In all cases, $f = 0.01$, $T = 0$ and $w_1 = 2$	66
20	The factor s_h as a function of h_a . The continuous line corresponds to equation (5.16) and the discrete points correspond to numerically determined values for various values of h_t . In all cases, $f = 0.01$, $T = 0$ and $w_1 = 2$	66
21	RVEs used for the unit cell calculations (a) prolate ($a_1/b_1 = 2$) (b) oblate ($a_1/b_1 = 1/2$). Porosity, $f = 0.01$ for both cases.	68
22	Evolution of porosity, f , with axial strain for an initially prolate cavity (a) FE simulation of porous unit cell (b) integration of constitutive equation. The material properties are taken from Table 1. The stress triaxiality was held constant at $T = 1$	69
23	Evolution of the void aspect ratio, w_1 , with axial strain for an initially prolate cavity (a) FE simulation of porous unit cell (b) integration of constitutive equation. The material properties are taken from Table 1. The stress triaxiality was held constant at $T = 1$	70

FIGURE	Page
24	Evolution of porosity, f , with axial strain for an initially oblate cavity (a) FE simulation of porous unit cell (b) integration of constitutive equation. The material properties are taken from Table 1. The stress triaxiality was held constant at $T = 1$ 72
25	Evolution of the void aspect ratio, w_1 , with axial strain for an initially oblate cavity (a) FE simulation of porous unit cell (b) integration of constitutive equation. The material properties are taken from Table 1. The stress triaxiality was held constant at $T = 1$ 73

CHAPTER I

INTRODUCTION

Alloys of Titanium (Ti) constitute some of the most important structural materials used in the aerospace industry due to favorable properties like high strength to weight ratio, high melting point and excellent corrosion resistance. Ti is approximately 40% lighter than steel while having comparable strength. This makes it ideal for use in those applications where light weight is a key design requirement. Trace quantities of alloying elements such as Aluminium and Vanadium significantly improves the mechanical properties of Ti. The alloy Ti-6Al-4V accounts for 50% of all alloys used in aerospace applications [4]. Ti alloys are extensively used in the manufacture of aircraft structural components, engine parts, landing gear, etc. Apart from its use in aerospace applications, Ti alloys also find use in defense equipment such as armored vehicles and tanks which are exposed to extreme operating conditions. The most notable chemical property of Ti is its high resistance to corrosive environments like acids and salt solutions. Hence Ti is used in marine applications like the manufacture of propeller shafts. Pure Ti has good bio-compatibility and is used in the design of implants and other medical and surgical equipment. Other applications of Ti include chemical and petro-chemical process industry, premium sports equipment and some consumer electronics devices.

Commercial production of Ti is similar to that of steel in the sense that the typical processing operations involved are casting followed by a series of primary and secondary hot working operations to produce the finished product. However, the processing of Ti alloys poses a significant technological challenge, since Ti is considerably

The journal model is *Comptes Rendus Mécanique*.

more difficult to hot work than steel due to its hexagonal crystal structure and sharp dependence of flow stress on temperature [2]. Typical hot working operations used in the manufacturing process are known to produce undesirable defects in the finished product such as microcracks, shear bands and porosity due to internal cavitation [2,5]. Figure 1 illustrates a typical “wedge crack” formed during hot working of a Ti alloy. The presence of such defects is the major cause of failure in Ti-based components.

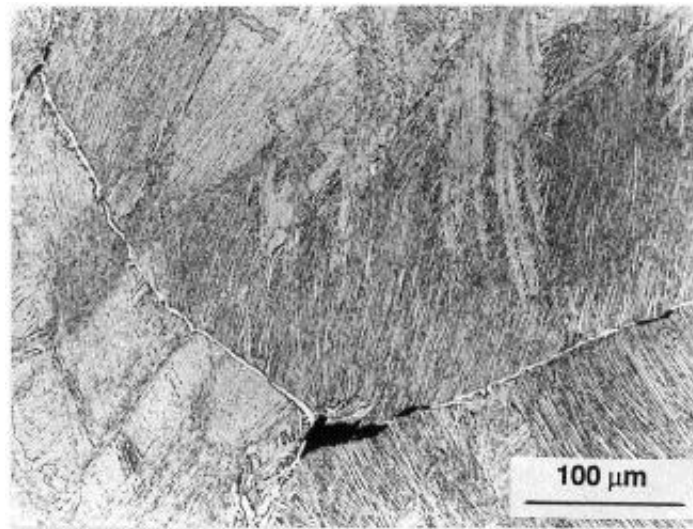


Fig. 1. Wedge crack formed at a grain boundary triple point during hot working of an α Ti-6Al-2Sn-4Zr-2Mo alloy. Micrograph from Semiatin et al. [2].

Therefore, the problem of determining optimal processing conditions or workability maps for Ti-alloys under various loading states is of high technological interest and one that was considered by several authors [6–8]. The results are usually presented in terms of graphs illustrating the reduction in area achieved in uniaxial tension tests at various temperatures and strain rates. Such maps are then used to determine safe strain rates that can be employed during hot working at various temperatures. However, since these maps are developed based on simple tensile or upset tests conducted at various temperatures, they may be expected to be accurate only for simple loading

states. On the other hand, the material often undergoes complex non-proportional loading paths under actual processing conditions, such as in rolling and extrusion. An alternative to experimental characterization of workability is computer based simulation of the actual processing operations, using numerical techniques like the finite element method. This option is increasingly being preferred due to its obvious cost advantage and widespread availability of computing resources.

However, accurate prediction of damage accumulation during plastic deformation requires use of a good constitutive model (yield criterion and flow rule) for the material under consideration. The α phase of Ti, which is dominant in Ti alloys at room temperature, has a hexagonal crystal structure which develops a textured microstructure leading to plastic flow anisotropy [9]. An ideal constitutive model should capture the evolution of the material texture for it to be representative of the material's actual response under external loading. In addition, large deformation plastic flow is associated with significant ductile damage accumulation in the form of microcracks and voids [10], which grow and evolve during the forming process. The macroscopic constitutive model should incorporate some of these microstructural details, like the porosity, void shape and orientation, and predict their evolution reasonably accurately. Developing a constitutive model incorporating the details of crystal plasticity of the anisotropic matrix coupled with damage growth, from first principles, is a challenging task. In this work, we attempt to couple the two effects using a simplified description of material anisotropy, which is modeled using the Hill quadratic yield criterion. The main emphasis is placed on faithful modeling of damage growth, i.e. the evolution of porosity and the void shape during plastic flow in an anisotropic matrix, since this is expected to be the key determinant that limits the formability of the material.

Another important application where accurate modeling of the material's plas-

tic response is of importance is the case of Ti components manufactured through the powder compaction process, which exhibit significant flow anisotropy due to the peculiar shape of the voids. Use of a simplified constitutive model to determine the reduction in porosity during the compaction process leads to poor agreement with the actual values observed [11], due to the fact that the models used are often phenomenological in nature and/or based on a simplistic description of the microstructure, like spherical voids. Use of a more sophisticated model that is developed from a rigorous micromechanical foundation and allows for non-spherical voids may be expected to yield better results in these cases.

Various plasticity models for materials with voids have been developed over the past few decades, starting with the works of McClintock [12], Rice and Tracey [13] and Gurson [14, 15] using the micromechanical approach. Alternative approaches to the problem have been explored in the works of Ponte Castaneda and Zaidman [16] using the non-linear variational principle developed by Ponte Castaneda [17], and that of Rousselier [18] using continuum thermodynamics. Among these works, Gurson's [15] has received the most attention due to its pioneering contribution to ductile fracture modeling, as he derived a closed form expression for the yield function of an isotropic porous material having a finite porosity and containing spherical voids. Gurson used a micromechanical rather than a phenomenological approach, basing his result on an approximate limit analysis of a porous representative volume element (RVE) made of a Von Mises matrix. Gurson's RVE consisted of a composite spheres assemblage with a void as the inclusion phase, and subjected to homogeneous deformation rate boundary conditions. Such an approach allowed him to derive a plastic potential for a material with finite porosity (albeit a small one), whereas previous models considered either growth of spherical holes in an infinite medium as in the Rice–Tracey model [13], or unrealistic void shapes like cylindrical through–thickness voids [12]. The novel

aspect of Gurson's result was that he derived a homogenized macroscopic constitutive relation that was substantially different from that of the individual phases. The form of the Gurson yield criterion, for spherical voids in an isotropic matrix, is shown below.

$$\mathcal{F}(\boldsymbol{\Sigma}) \equiv \frac{\Sigma_{eq}^2}{\sigma_0^2} + 2f \cosh \frac{3}{2} \frac{\Sigma_m}{\sigma_0} - 1 - f^2 = 0, \quad \Sigma_{eq} \equiv \sqrt{\frac{3}{2} \boldsymbol{\Sigma}' : \boldsymbol{\Sigma}'} \quad (1.1)$$

where Σ_m and $\boldsymbol{\Sigma}'$ represents the mean and deviatoric parts of the macroscopic stress tensor, $\boldsymbol{\Sigma}$, Σ_{eq} denotes the Von Mises effective stress and f represents the porosity. Notice that the criterion depends on the mean macroscopic stress through the ‘‘cosh’’ term, which when combined with a normality flow rule results in an exponential growth of the porosity with the mean stress. For a sound material, with porosity $f = 0$, the criterion reduces to the Von Mises yield criterion.

The success of the Gurson model, as it is known in the literature, could be attributed to the fact that the result represented a rigorous upper bound, which also happened to lie close to the true yield locus. It may be noted that the former was not apparent initially and some of the approximations used in Gurson's original derivations suggested the contrary. However, it was established much later by Leblond and Perrin [19] that the Gurson criterion could be derived based on a homogenization and limit analysis approach that resulted in a rigorous upper bound for the true yield criterion. Many of the later works have followed a similar micromechanical approach and extended Gurson's results to include plastic anisotropy of the matrix [20–22] and void shape effects [23–27]. The objective of the present work is to develop a unified constitutive model of anisotropic porous plastic materials, based on rigorous micromechanical analysis, and incorporating the effects of plastic anisotropy of the matrix and void shape effects in the spirit of the above mentioned works. In particular, the development of the model follows closely the works of Gologanu et al. [25] on void

shape effects and Benzerga and Besson [22] on plastic anisotropy.

It may be mentioned here that a similar problem was considered recently by Monchiet et al. [3, 28], who developed a yield criterion for porous materials containing spheroidal voids in an anisotropic Hill matrix, following the approach of the earlier works of Gologanu et al. [23, 24]. However, finite element simulations on porous unit cells, containing spheroidal voids in an isotropic matrix, conducted by Sovik [29] had revealed some discrepancies with the model predictions of Gologanu et al. [23, 24] in relation to the evolution of porosity and void shape. Based on these findings, Gologanu et al. have proposed an improved criterion using an enhanced description of the admissible deformation fields in the material [25]. In our work, we have chosen to follow this approach and replace the isotropic Von Mises matrix by an orthotropic matrix obeying the Hill criterion. Our numerical analysis, presented in chapter IV, indicates that this approach results in an improved agreement between the analytical and the numerical yield loci vis-a-vis the criterion of Monchiet et al. [3]. The trade-off in adopting this approach is that the enhanced description of the deformation field greatly increases the mathematical complexity of the subsequent analysis. This necessitates introduction of a set of approximations, which do not always preserve the upper bound character of the resulting yield criterion. However, our numerical results reveal that the new approximate criterion provides better agreement with the true yield loci than the criterion of Monchiet et al. in the cases of small porosity and practical range of values of the anisotropy parameters for the matrix.

The remainder of this thesis is organized as follows. The second chapter provides a brief introduction to the fields of homogenization and limit analysis. The treatment is in no way exhaustive, and the scope is limited to presentation of those results that are directly relevant to the development of our model, with references to the literature cited at appropriate places. The third chapter contains the definition of

the homogenization problem, followed by derivation of the analytical yield criterion based on results presented in the second chapter. Emphasis is placed on presentation of the logical sequence of the derivations, discussion of the main assumptions, related approximations and the results. The fourth chapter presents the details of the numerical limit analysis procedure used to derive the “exact” numerical yield loci, followed by a discussion of the results, including comparisons of the analytical and numerical yield loci. The evolution equations for the internal variables, porosity and void shape parameter, are derived in the fifth chapter. The constitutive equations are integrated for specific loading paths, and the results are compared with finite element simulations of porous unit cells for validation of the evolution laws. Finally, we discuss heuristic generalizations of the model to arbitrary loading states in the final chapter, followed by our conclusions.

CHAPTER II

HOMOGENIZATION AND LIMIT ANALYSIS

This chapter presents a brief introduction to the main results from homogenization and limit analysis that form the theoretical basis for the derivations presented in subsequent chapters. Homogenization is the process by which the microscopic fields at the scale of the material microstructure are averaged out to obtain a constitutive relation that is representative of the material's response at the macro scale, which is typically several orders of magnitude larger than the scale of the microstructure. For a porous material, the micro scale corresponds to the scale of the voids, which are typically micron-sized, while the macro scale may be the size of the specimen which is usually of the order of millimeters or higher. The homogenized constitutive relation at the macro scale will contain some information of the microstructure, like the volume fraction of the voids for a porous material, in the form of internal variables. Limit analysis is a subfield of plasticity theory, where general results about an elastic-plastic solid are obtained using variational principles *without* having a complete knowledge of the microscopic fields in the material. Typically, limit analysis is used to derive bounds and estimates for the quantities of interest in an engineering problem, like the limit loads for an elasto-plastic beam, without having to solve the complete boundary value problem. In conjunction with homogenization theory, limit analysis performed on a micromechanical RVE can be used to derive constitutive relations for a composite material undergoing plastic deformation, as illustrated in the following sections in the context of a porous material containing a distribution of voids in a rigid perfectly plastic matrix.

A. Hill-Mandel Homogenization Theory

Consider a representative volume element (RVE) of a porous material as shown in figure 2. Here ω represents the total volume of the voids and Ω the volume of the RVE (matrix + voids). The RVE is chosen such that the void volume fraction, $f \equiv \omega/\Omega$, is representative of that of the material. Required is the average constitutive response

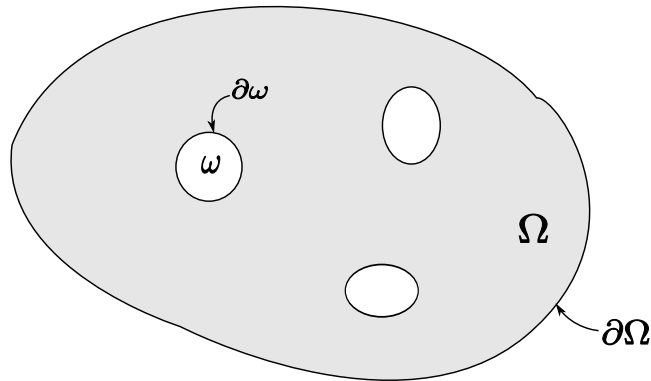


Fig. 2. Sketch of a porous representative volume element.

of the RVE to the macroscopic imposed fields, which translates into appropriate boundary conditions specified on $\partial\Omega$, the boundary of the RVE. Considering that the scale of the RVE is several orders of magnitude smaller than that of the specimen, one may neglect the gradients of the macroscopic fields at the scale of the RVE in the first approximation. Hence, the problem reduces to determination of the response of the RVE subject to homogeneous stress or deformation-rate boundary conditions on $\partial\Omega$. (Note that only one of the two can be imposed on any given part of the boundary of the RVE, $\partial\Omega$). The term “homogeneous” here signifies that the form of the tractions or velocities on $\partial\Omega$ is the same as if the stress or deformation-rate field in the RVE were homogeneous. I.e.,

$$\forall \quad \mathbf{x} \in \partial\Omega, \quad \mathbf{t}(\mathbf{x}) = \boldsymbol{\sigma}(\mathbf{x}) \cdot \mathbf{n}(\mathbf{x}) = \boldsymbol{\Sigma} \cdot \mathbf{n}(\mathbf{x}) \quad (2.1)$$

for homogeneous stress boundary conditions, and

$$\forall \quad \mathbf{x} \in \partial\Omega, \quad \mathbf{v}(\mathbf{x}) = \mathbf{D} \cdot \mathbf{x} \quad (2.2)$$

for homogeneous rate of deformation on the boundary. Here, $\boldsymbol{\sigma}$ and \mathbf{d} represent the microscopic stress and deformation-rate fields respectively, while $\boldsymbol{\Sigma}$ and \mathbf{D} denote the corresponding imposed macroscopic fields on the boundary. The boundary condition on $\partial\omega$ corresponds to the traction free condition, i.e. $\boldsymbol{\sigma}(\mathbf{x}) \cdot \mathbf{n}(\mathbf{x}) = \mathbf{0}$ on $\partial\omega$.

In the Hill-Mandel [30, 31] homogenization theory, the macroscopic stress and deformation rate fields for the RVE are defined as the volume average over the RVE of the corresponding microscopic fields. I.e.,

$$\boldsymbol{\Sigma} \equiv \langle \boldsymbol{\sigma}(\mathbf{x}) \rangle_{\Omega}, \quad \mathbf{D} \equiv \langle \mathbf{d}(\mathbf{x}) \rangle_{\Omega} \quad (2.3)$$

where the notation $\langle \cdot \rangle_{\Omega}$ represents the volume average over the RVE. It is then straightforward to show, using the divergence theorem, that the quantities $\boldsymbol{\Sigma}$ and \mathbf{D} of equation (2.3) are equal to the imposed macroscopic fields $\boldsymbol{\Sigma}$ and \mathbf{D} of equations (2.1) and (2.2), for homogeneous stress and deformation-rate boundary conditions respectively. Again, employing the virtual velocities theorem in conjunction with the divergence theorem, one can proceed to show that these two quantities are work conjugate, i.e.,

$$\boldsymbol{\Sigma} : \mathbf{D} = \langle \boldsymbol{\sigma} \rangle_{\Omega} : \langle \mathbf{d} \rangle_{\Omega} = \langle \boldsymbol{\sigma} : \mathbf{d} \rangle_{\Omega} \quad (2.4)$$

The above result is known as the **Hill-Mandel lemma**, which will be used later to derive an upper bound for the macroscopic yield criterion.

A few caveats may be mentioned for the case of a porous material. In this case, the microscopic fields, $\boldsymbol{\sigma}$ and \mathbf{d} , are not defined within the voids. Nevertheless, one can show that all the theorems discussed above hold regardless of the extension chosen

for $\boldsymbol{\sigma}$ and \mathbf{d} in ω as long as the continuity of tractions and velocities across $\partial\omega$ is preserved. Also, it may be noted that the macroscopic deformation field \mathbf{D} defined by (2.3) need not be traceless, even if the matrix is assumed to be incompressible, due to the possible expansion of the voids (and hence $\partial\omega$).

B. Limit Analysis of the Macroscopic Yield Criterion

As mentioned previously, the field of limit analysis deals with determination of bounds and estimates of the quantities of interest for an elasto-plastic material, using variational principles. Limit analysis is useful in those instances where the actual boundary value problem may be too difficult to solve, as is usually the case in problems involving nonlinear material behavior like plasticity, and full knowledge of the deformation fields is not required. A typical example is determination of the limit load for an elasto-plastic beam, i.e. the load at which the beam undergoes unbounded plastic deformation. In the context of homogenization theory, limit analysis can be used to derive bounds for the yield criterion of an elasto-plastic composite. A detailed treatment of homogenization and limit analysis may be found in [32, 33]. The scope of the treatment here will be restricted to presentation of the theorems of limit analysis that are used in the derivation of an upper bound for the macroscopic yield locus of a porous material. Some of the expected features of the sought for yield criterion may be noted. *A priori*, the yield criterion may be expected to depend on the mean macroscopic pressure, unlike for a sound plastic material. Also, the macroscopic plastic deformation field derived from the yield criterion through the associated flow rule need not be incompressible due to the possible expansion of the holes.

Considering again the RVE sketched in figure 2, we now assume that the matrix is made of a rigid-ideal plastic orthotropic material that obeys the Hill quadratic yield

criterion [34]. The space of admissible stresses is a convex region, \mathcal{C} , in stress space given by

$$\sigma_{eq} \equiv \sqrt{\frac{3}{2} \boldsymbol{\sigma} : \mathbf{p} : \boldsymbol{\sigma}} = \sqrt{\frac{3}{2} \boldsymbol{\sigma}' : \mathbf{h} : \boldsymbol{\sigma}'} \leq \sigma_1, \quad \mathbf{p} = \mathbf{J} : \mathbf{h} : \mathbf{J} \quad (2.5)$$

where σ_{eq} is called the “equivalent” (or “effective”) stress, \mathbf{p} is the Hill tensor which represents the anisotropy of the material, $\boldsymbol{\sigma}'$ is the stress deviator, and σ_1 is the yield stress in one of the directions of orthotropy, chosen arbitrarily. Since the criterion is independent of pressure ($p_{iikl} = 0$), the tensor \mathbf{p} admits a definition in terms of the anisotropy tensor \mathbf{h} [22] through the relation shown above involving the deviatoric projection operator $\mathbf{J} \equiv \mathbf{I}_4 - \frac{1}{3} \mathbf{I}_2 \otimes \mathbf{I}_2$ ($\mathbf{I}_4 =$ fourth order identity tensor, $\mathbf{I}_2 =$ second order identity tensor). The tensor \mathbf{p} (and consequently \mathbf{h}) obeys the symmetries $p_{ijkl} = p_{jikl} = p_{ijlk} = p_{klij}$. In the frame of material orthotropy, \mathbf{h} may be represented as a diagonal 6×6 matrix, whose diagonal elements are denoted h_i . In fact, only five of the six diagonal elements are independent, since the values of h_i are normalized such that the quadratic form for σ_{eq} equals the yield stress in one of the orthotropy directions. The **microscopic plastic dissipation** for a given microscopic deformation field \mathbf{d} , is defined by

$$\pi(\mathbf{d}) \equiv \sup_{\boldsymbol{\sigma}^* \in \mathcal{C}} \boldsymbol{\sigma}^* : \mathbf{d} \quad (2.6)$$

The supremum is taken over all stresses that fall within the microscopic convex of rigidity, \mathcal{C} , defined by equation (2.5). Performing the above maximization one can show that, for a Hill orthotropic material

$$\pi(\mathbf{d}) = \sigma_1 d_{eq}, \quad d_{eq} \equiv \sqrt{\frac{2}{3} \mathbf{d} : \hat{\mathbf{h}} : \mathbf{d}} \quad (2.7)$$

where d_{eq} is called the microscopic “equivalent” (or “effective”) strain rate, work conjugate with σ_{eq} . $\hat{\mathbf{h}}$ is the formal inverse of the \mathbf{h} tensor, obtained from the relation

$\hat{\mathbf{h}} = \mathbf{J} : \hat{\mathbf{p}} : \mathbf{J}$ with $\hat{\mathbf{p}}$ given by $\mathbf{p} : \hat{\mathbf{p}} = \hat{\mathbf{p}} : \mathbf{p} = \mathbf{J}$ [22].

Let $\boldsymbol{\sigma}(\mathbf{x})$ represent a statically admissible stress field in the RVE of figure 2, i.e. $\sigma_{ij,j} = 0$, $\boldsymbol{\sigma} \cdot \mathbf{n} = 0$ on $\partial\omega$ and $\boldsymbol{\sigma} \cdot \mathbf{n} = \boldsymbol{\Sigma} \cdot \mathbf{n}$ on $\partial\Omega$ (for homogeneous boundary stress) or $\langle \boldsymbol{\sigma} \rangle_{\Omega} = \boldsymbol{\Sigma}$ (for homogeneous boundary strain rate). Let \mathbf{d} be a kinematically admissible deformation field, i.e. satisfying $d_{ii} = 0$ (incompressibility) and $\mathbf{d} \cdot \mathbf{x} = \mathbf{D} \cdot \mathbf{x}$ on $\partial\Omega$ (for homogeneous boundary strain rate) or $\langle \mathbf{d} \rangle_{\Omega} = \mathbf{D}$ (for homogeneous boundary stress). Using the Hill-Mandel lemma (2.4) and the definition of the microscopic plastic dissipation (2.6), we have

$$\boldsymbol{\Sigma} : \mathbf{D} = \langle \boldsymbol{\sigma} : \mathbf{d} \rangle_{\Omega} \leq \langle \pi(\mathbf{d}) \rangle_{\Omega} \quad (2.8)$$

The above inequality is true for any kinematically admissible velocity field and hence

$$\boldsymbol{\Sigma} : \mathbf{D} \leq \inf_{\mathbf{d} \in \mathcal{K}(\mathbf{D})} \langle \pi(\mathbf{d}) \rangle_{\Omega} \equiv \Pi(\mathbf{D}) \quad (2.9)$$

where $\mathcal{K}(\mathbf{D})$ denotes the set of microscopic deformation fields kinematically admissible with \mathbf{D} . $\Pi(\mathbf{D})$ is termed the **macroscopic plastic dissipation** associated with \mathbf{D} . The above inequality implies that of all the admissible deformation fields in the RVE, the true field minimizes the functional $\Pi(\mathbf{D})$. Equation (2.9) is a statement of the **principle of minimum plastic dissipation** of limit analysis applied to a micromechanical RVE, and allows us to derive an upper bound for the macroscopic yield locus of the RVE.

For a given \mathbf{D} , equation (2.9) represents a half-space in the macroscopic stress space. It then follows that the domain of potentially supportable macroscopic stresses (macroscopic convex of rigidity) is the region that lies at the intersection of all such half-spaces (for all \mathbf{D}) [32]. The macroscopic yield locus is then the envelope of the hyper-planes $\boldsymbol{\Sigma} : \mathbf{D} = \Pi(\mathbf{D})$ in stress space, with \mathbf{D} as the parameter. A consequence of the above result is that the macroscopic yield locus is convex. We have from (2.7)

that the microscopic plastic dissipation, $\pi(\mathbf{d})$, is positively homogeneous of degree 1 in the components of \mathbf{d} , which implies that $\Pi(\mathbf{D})$ is also positively homogeneous of degree 1 in the components of \mathbf{D} . Therefore, $\Pi(\mathbf{D})$ obeys the following Euler relation

$$\frac{\partial \Pi}{\partial \mathbf{D}} : \mathbf{D} = \Pi(\mathbf{D}) \quad (2.10)$$

Differentiating the relation $\Sigma : \mathbf{D} = \Pi(\mathbf{D})$ with respect to \mathbf{D} , we have

$$\Sigma - \frac{\partial \Pi}{\partial \mathbf{D}} = 0 \quad (2.11)$$

Equations (2.10) and (2.11) together yields the result that the parametric equation of the macroscopic yield surface is given by

$$\Sigma = \frac{\partial \Pi}{\partial \mathbf{D}}(\mathbf{D}) \quad (2.12)$$

with \mathbf{D} as the parameter. Note that since $\Pi(\mathbf{D})$ is homogeneous of degree 1 on the components of \mathbf{D} , $\partial \Pi / \partial \mathbf{D}$ is homogeneous of degree zero, i.e. Σ depends on the five ratios of the components of \mathbf{D} . Thus, equation (2.12) represents a 5-D surface in a 6-D space. Elimination of these ratios between the six equations (2.12) yields the explicit equation of the macroscopic yield locus.

Use of equation (2.12) to determine an expression for the macroscopic yield locus requires the minimization of the functional, $\Pi(\mathbf{D})$, given by (2.9) over an infinite number of kinematically admissible velocity fields. In practice, a finite number of admissible velocity fields are used and equation (2.9) guarantees that the resulting expression is an upper bound for the actual $\Pi(\mathbf{D})$, denoted $\Pi^+(\mathbf{D})$. It then follows that the envelope of the hyper-planes $\Sigma : \mathbf{D} = \Pi^+(\mathbf{D}) \geq \Pi(\mathbf{D})$ is a convex hyper-surface that is external to the true yield surface.

CHAPTER III

APPROXIMATE ANALYTICAL YIELD CRITERION FOR ANISOTROPIC
POROUS MEDIA

The homogenization and limit analysis approach presented in the previous chapter is now used to derive an approximate analytical yield criterion for a porous spheroidal RVE made of an orthotropic Hill matrix, containing a single confocal spheroidal void. The RVE geometry is a generalization of the composite spheres model used by Gurson [15] and was used in the previous works on void shape effects [3, 23–25]. Two different void shapes are considered, namely prolate and oblate voids. Admittedly, this choice of the void shape is an approximation and a better choice would have been to consider the more general case of ellipsoidal voids, with two associated shape parameters. However, this will require a fully three dimensional description of the velocity fields, and the calculations involved are not tractable analytically. In spite of this limitation, it may be mentioned that the spheroidal shape is representative of a variety of actual void shapes observed, ranging from penny shaped cracks (limiting case of oblate voids) to needle shaped voids (limit of prolate shaped voids). Following Gologanu et al. [25], we make two additional assumptions that considerably simplify the derivation of the analytical yield locus:

1. The macroscopic loading is assumed to be axisymmetric about the axis of symmetry of the RVE. The resulting yield criterion will then be expressed in terms of the two independent principal components of the macroscopic stress tensor. We propose a heuristic generalization of this criterion to general cases of loading in chapter VI.
2. The RVE is assumed to deform axisymmetrically and the void is assumed to

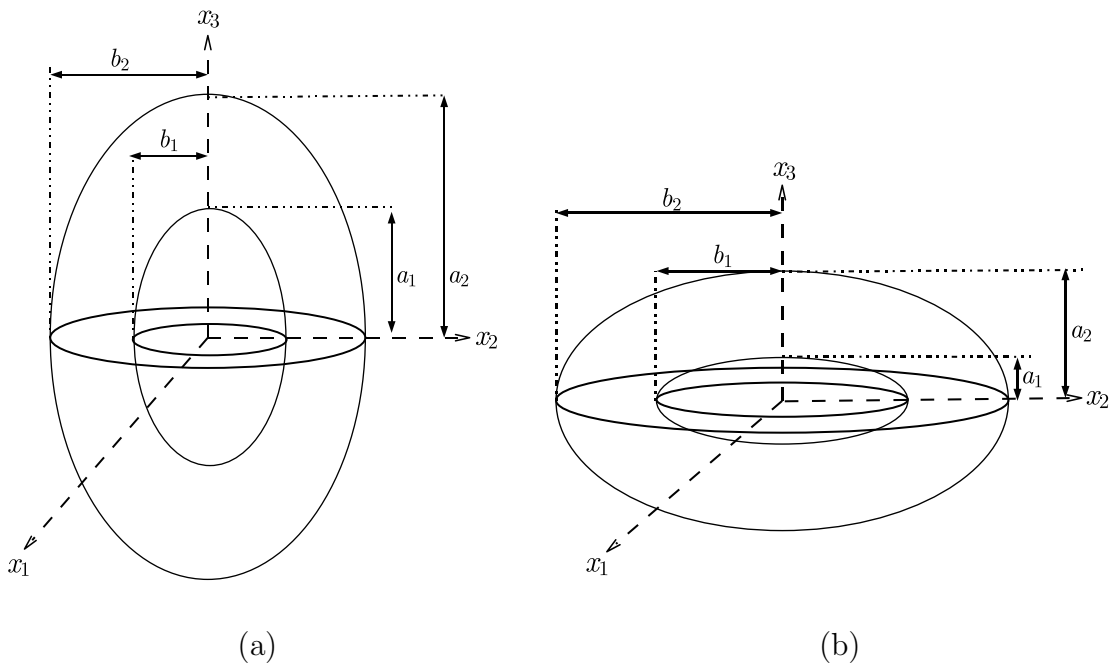


Fig. 3. Porous RVEs considered (a) prolate (b) oblate.

remain approximately spheroidal throughout the deformation. This is obviously not true for the general cases of loading and material orthotropy. However, as discussed in chapter II, equations (2.9) and (2.12) guarantee that the resulting yield locus is an upper bound to the true yield locus. Thus, this approximation preserves the upper bound character of the approach.

A. Geometry and Coordinates

Consider a prolate or oblate spheroidal RVE containing a confocal spheroidal void, as illustrated in figure 3. Let Ω and ω represent the volume of the RVE and the void respectively, and let c represent the semi-focal length of the spheroids, given by $c = \sqrt{|a_1^2 - b_1^2|} = \sqrt{|a_2^2 - b_2^2|}$. Since the problem is scale independent, the geometry is completely defined by two parameters, namely the porosity $f = \omega/\Omega$ and the void shape parameter, $S = \ln w_1$, where w_1 is the void aspect ratio defined by $w_1 = a_1/b_1$.

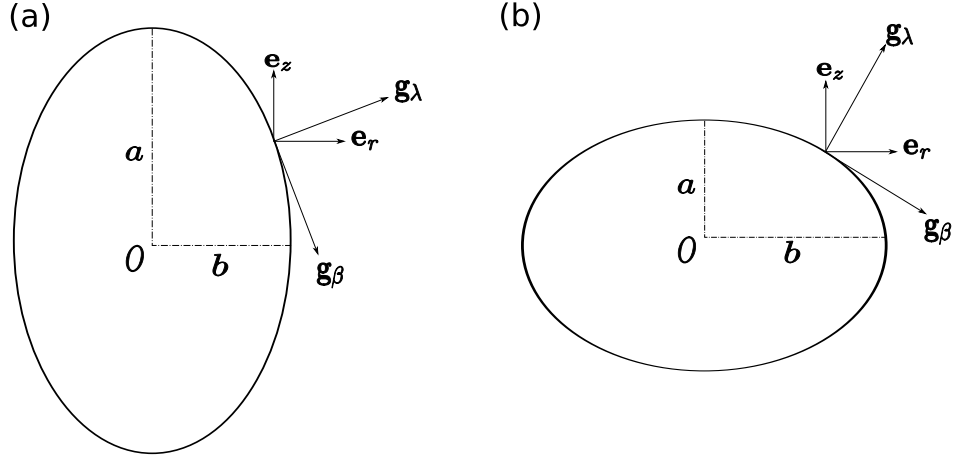


Fig. 4. Base vectors of the spheroidal curvilinear coordinate system (a) prolate (b) oblate.

Thus, we have $S > 0$ for prolate voids and $S < 0$ for oblate voids.

Due to the spheroidal geometry of the problem being considered, it is most convenient to express the microscopic fields and the boundary conditions using spheroidal coordinates $(\lambda, \beta, \varphi)$, associated with the natural basis $(\mathbf{g}_\lambda, \mathbf{g}_\beta, \mathbf{g}_\varphi)$ (see figure 4).

These are defined in an orthonormal cylindrical basis $(\mathbf{e}_r, \mathbf{e}_\theta, \mathbf{e}_z)$, with \mathbf{e}_z aligned with the symmetry axis of the spheroid, as

$$\begin{aligned}
 \mathbf{g}_\lambda &= a \sin \beta \mathbf{e}_r + b \cos \beta \mathbf{e}_z \\
 \mathbf{g}_\beta &= b \cos \beta \mathbf{e}_r - a \sin \beta \mathbf{e}_z \\
 \mathbf{g}_\varphi &= b \sin \beta \mathbf{e}_\theta
 \end{aligned} \tag{3.1}$$

where a and b represent the semi-axes of the current spheroid, given by

$$\begin{aligned}
 a &= c \cosh \lambda, \quad b = c \sinh \lambda, \quad e = c/a = 1/\cosh \lambda & \text{(p)} \\
 a &= c \sinh \lambda, \quad b = c \cosh \lambda, \quad e = c/b = 1/\cosh \lambda & \text{(o)}
 \end{aligned} \tag{3.2}$$

and e denotes the eccentricity. The notation (p) and (o) above represent prolate and oblate spheroids respectively. The covariant components of the metric tensor are obtained from the relation $g_{ij} = \mathbf{g}_i \cdot \mathbf{g}_j$. The non-zero components of the metric tensor

are

$$\begin{aligned} g_{\lambda\lambda} &= g_{\beta\beta} = a^2 \sin^2 \beta + b^2 \cos^2 \beta \\ g_{\varphi\varphi} &= b^2 \sin^2 \beta \end{aligned} \quad (3.3)$$

and the Lamé coefficients are given by

$$L_\lambda = \sqrt{g_{\lambda\lambda}}, \quad L_\beta = \sqrt{g_{\beta\beta}}, \quad L_\varphi = \sqrt{g_{\varphi\varphi}} \quad (3.4)$$

The iso- λ surfaces are confocal spheroids of focal length $2c$ and the iso- β surfaces are confocal hyperboloids of revolution orthogonal to the iso- λ surfaces. In particular, the boundaries of the void and the RVE are given by constant values of λ , designated λ_1 and λ_2 (eccentricities e_1 and e_2) respectively.

B. Incompressible Axisymmetric Velocity Fields of Lee and Mear

As discussed at the beginning of the chapter, we consider only axisymmetric velocity fields, primarily due to the fact that this considerably simplifies the algebra involved in the limit analysis. Since the matrix is assumed to be plastically incompressible, the microscopic velocity fields considered must be incompressible, i.e. $\text{tr}(\mathbf{d}) = 0$. In spheroidal coordinates, the covariant components of the deformation rate tensor, \mathbf{d} , are given by

$$\left\{ \begin{aligned} d_{\lambda\lambda} &= \frac{\partial v_\lambda}{\partial \lambda} - \frac{c^2 \sinh \lambda \cosh \lambda}{L_\lambda^2} v_\lambda + \frac{c^2 \sin \beta \cos \beta}{L_\lambda^2} v_\beta \\ d_{\beta\beta} &= \frac{\partial v_\beta}{\partial \beta} + \frac{c^2 \sinh \lambda \cosh \lambda}{L_\lambda^2} v_\lambda - \frac{c^2 \sin \beta \cos \beta}{L_\lambda^2} v_\beta \\ d_{\varphi\varphi} &= \frac{L_\varphi^2}{L_\lambda^2} (v_\lambda \coth \lambda + v_\beta \cot \beta) \\ d_{\lambda\beta} &= \frac{1}{2} \left(\frac{\partial v_\lambda}{\partial \beta} + \frac{\partial v_\beta}{\partial \lambda} \right) - \frac{c^2}{L_\lambda^2} (v_\lambda \sin \beta \cos \beta + v_\beta \sinh \lambda \cosh \lambda) \\ d_{\lambda\varphi} &= d_{\beta\varphi} = 0 \end{aligned} \right. \quad (\text{p}) \quad (3.5)$$

for the prolate case and

$$\left\{ \begin{array}{l} d_{\lambda\lambda} = \frac{\partial v_\lambda}{\partial \lambda} - \frac{c^2 \sinh \lambda \cosh \lambda}{L_\lambda^2} v_\lambda - \frac{c^2 \sin \beta \cos \beta}{L_\lambda^2} v_\beta \\ d_{\beta\beta} = \frac{\partial v_\beta}{\partial \beta} + \frac{c^2 \sinh \lambda \cosh \lambda}{L_\lambda^2} v_\lambda + \frac{c^2 \sin \beta \cos \beta}{L_\lambda^2} v_\beta \\ d_{\varphi\varphi} = \frac{L_\lambda^2}{L_\lambda^2} (v_\lambda \coth \lambda + v_\beta \cot \beta) \\ d_{\lambda\beta} = \frac{1}{2} \left(\frac{\partial v_\lambda}{\partial \beta} + \frac{\partial v_\beta}{\partial \lambda} \right) + \frac{c^2}{L_\lambda^2} (v_\lambda \sin \beta \cos \beta - v_\beta \sinh \lambda \cosh \lambda) \\ d_{\lambda\varphi} = d_{\beta\varphi} = 0 \end{array} \right. \quad (\text{o}) \quad (3.6)$$

for the oblate case. In the above expressions, v_i are the covariant components of the microscopic velocity field (associated with the dual basis \mathbf{g}^i defined by $\mathbf{g}^i \cdot \mathbf{g}_j = \delta_{ij}$). Therefore, the incompressibility condition in spheroidal coordinates becomes

$$\frac{\partial v_\lambda}{\partial \lambda} + \frac{\partial v_\beta}{\partial \beta} + v_\lambda \coth \lambda + v_\beta \cot \beta = 0 \quad (3.7)$$

Lee and Mear [35] have proposed a general solution to the above equation, which supposedly represents the complete set of axisymmetric incompressible velocity fields.

The components of the Lee-Mear fields in spheroidal coordinates writes

$$\left\{ \begin{array}{l} v_\lambda(\lambda, \beta) = c^2 \{ B_{00} / \sinh(\lambda) \\ + \sum_{k=2,4,\dots}^{+\infty} \sum_{m=0}^{+\infty} k(k+1) [B_{km} Q_m^1(w) + C_{km} P_m^1(w)] P_k(u) \} \\ v_\beta(\lambda, \beta) = c^2 \{ \sum_{k=2,4,\dots}^{+\infty} \sum_{m=1}^{+\infty} m(m+1) [B_{km} Q_m(w) \\ + C_{km} P_m(w)] P_k^1(u) \} \end{array} \right. \quad (\text{p}) \quad (3.8)$$

$$\left\{ \begin{array}{l} v_\lambda(\lambda, \beta) = c^2 \{ B_{00} / \cosh(\lambda) \\ + \sum_{k=2,4,\dots}^{+\infty} \sum_{m=0}^{+\infty} k(k+1) i^m [i B_{km} Q_m^1(w) + C_{km} P_m^1(w)] P_k(u) \} \\ v_\beta(\lambda, \beta) = c^2 \{ \sum_{k=2,4,\dots}^{+\infty} \sum_{m=1}^{+\infty} m(m+1) i^m [i B_{km} Q_m(w) \\ + C_{km} P_m(w)] P_k^1(u) \} \end{array} \right. \quad (\text{o}) \quad (3.9)$$

where,

$$w \equiv \begin{cases} \cosh \lambda & \text{(p)} \\ i \sinh \lambda & \text{(o)} \end{cases} ; \quad u \equiv \cos \beta \quad (3.10)$$

In the above expressions, P_n^m and Q_n^m represent associated Legendre functions of the first and second kinds respectively, of order m and degree n [36], and B_{ij} and C_{ij} are arbitrary real constants.

C. Derivation of the Approximate Analytical Criterion

1. Boundary Conditions

As the first step in the derivation of an approximate analytical yield criterion for the RVE of figure 3, we need to derive an expression for the macroscopic plastic dissipation, $\Pi(\mathbf{D})$. This requires evaluation of the infimum of equation (2.9) over a set of kinematically admissible velocity fields. We choose a subset of the Lee-Mear fields, equations (3.8-3.9), to represent the microscopic deformation field, so that the condition of plastic incompressibility is automatically satisfied. The boundary conditions at the remote boundary, $\partial\Omega$, imposes further constraints on the velocity fields. It has been shown by Leblond and Perrin [19] that the choice of homogeneous deformation-rate boundary conditions leads to a rigorous upper bound, and is preferable to homogeneous stress boundary conditions. Hence, following the previous works [22, 25], we impose homogeneous (axisymmetric) deformation rate boundary conditions, which writes

$$\begin{aligned} \mathbf{D} &= D_{11} (\mathbf{e}_1 \otimes \mathbf{e}_1 + \mathbf{e}_2 \otimes \mathbf{e}_2) + D_{33} \mathbf{e}_3 \otimes \mathbf{e}_3 \\ \forall \quad \mathbf{x} \in \partial\Omega, \quad \mathbf{v} &= \mathbf{D} \cdot \mathbf{x} \end{aligned} \quad (3.11)$$

where $(\mathbf{e}_1, \mathbf{e}_2, \mathbf{e}_3)$ is a Cartesian basis with \mathbf{e}_3 aligned with the void axis and the directions of \mathbf{e}_1 and \mathbf{e}_2 chosen arbitrarily (see figure 3). Using spheroidal coordinates,

the two independent components of the above equation become

$$\begin{aligned} v_\lambda(\lambda = \lambda_2, \beta) &= a_2 b_2 (D_m + D'_{33} P_2(u)) \\ v_\beta(\lambda = \lambda_2, \beta) &= (a_2^2 D_{33} - b_2^2 D_{11}) P_2^1(u) / 3 \end{aligned} \quad (3.12)$$

where D_m and \mathbf{D}' denote the mean and deviatoric parts of the deformation tensor respectively. Since the associated Legendre functions are linearly independent and the coefficients B_{ij} and C_{ij} are arbitrary, comparison with equations (3.8) and (3.9) yields

$$\begin{aligned} c^3 B_{00} &= a_2 b_2^2 D_m; & 6c^2 F_2(\lambda_2) &= a_2 b_2 D'_{33}; & 3c^2 G_2(\lambda_2) &= a_2^2 D_{33} - b_2^2 D_{11}; \\ F_k(\lambda_2) &= G_k(\lambda_2) = 0, & k &= 4, 6, 8, \dots \end{aligned} \quad (3.13)$$

where,

$$\begin{cases} F_k(\lambda) \equiv \sum_{m=0}^{+\infty} [B_{km} Q_m^1(w) + C_{km} P_m^1(w)] \\ G_k(\lambda) \equiv \sum_{m=1}^{+\infty} m(m+1) [B_{km} Q_m(w) + C_{km} P_m(w)] \end{cases} \quad \text{(p)} \quad (3.14)$$

$$\begin{cases} F_k(\lambda) \equiv \sum_{m=0}^{+\infty} i^m [i B_{km} Q_m^1(w) + C_{km} P_m^1(w)] \\ G_k(\lambda) \equiv \sum_{m=1}^{+\infty} m(m+1) i^m [i B_{km} Q_m(w) + C_{km} P_m(w)] \end{cases} \quad \text{(o)}$$

Eliminating D_{11} and D_{33} between the three equations (3.13)₁ yields the following equations

$$\begin{cases} e_2^3 B_{00} / (3(1 - e_2^2)) + (3 - e_2^2) F_2(\lambda_2) / \sqrt{1 - e_2^2} - G_2(\lambda_2) = 0 & \text{(p)} \\ -e_2^3 B_{00} / (3\sqrt{1 - e_2^2}) + (3 - 2e_2^2) F_2(\lambda_2) / \sqrt{1 - e_2^2} - G_2(\lambda_2) = 0 & \text{(o)} \end{cases} \quad (3.15)$$

Equations (3.13)₂ and (3.15) constitute linear constraints on the space of admissible values of B_{ij} and C_{ij} , corresponding to the condition of homogeneous axisymmetric strain rate on the RVE boundary, $\partial\Omega$.

2. Choice of Velocity Fields

The approach followed in Gurson’s work [15] and later works based on it [3, 22–24] was to use two trial velocity fields so that the need for explicit minimization of $\Pi(\mathbf{D})$ is eliminated. This is because the two independent components of the imposed macroscopic deformation field completely determines the multiplicative factors of these velocity fields. However, this approach was found to have some limitations in the case of spheroidal voids. The model predictions for porosity and void shape evolution using the two field approach was found to be in poor agreement with direct finite element calculations on porous unit cells [25]. Gologanu et al. [25] have proposed an improved yield criterion that remedies some of these defects, using an enhanced description of the deformation field derived from the Lee-Mear decomposition. Since these considerations also apply in the present case (as the case of a Von Mises matrix considered by [25] is a special case of the Hill matrix being considered here), we have chosen to follow the extended approach of Gologanu et al. [25]. Specifically, we use the same Lee-Mear field components employed by these authors and described below.

First, the microscopic velocity field, \mathbf{v} , is decomposed into a uniform deviatoric strain rate field, \mathbf{v}^B , and a non-homogeneous field, \mathbf{v}^A , responsible for the expansion of the voids. i.e.

$$\mathbf{v} = A\mathbf{v}^A + B\mathbf{v}^B \quad (3.16)$$

where

$$\mathbf{v}^B = -\frac{x_1}{2}\mathbf{e}_1 - \frac{x_2}{2}\mathbf{e}_2 + x_3\mathbf{e}_3 \quad (3.17)$$

The expansion field, \mathbf{v}^A , is chosen as a linear combination of four Lee-Mear field components corresponding to the coefficients B_{00} , B_{20} , B_{21} and B_{22} in equations (3.8)–(3.9). The coefficient B_{00} taken as unity to “normalize” the field \mathbf{v}^A . The remaining coefficients, collectively referred to as B_{2i} , are left undefined, to be fixed later indepen-

dently of the boundary conditions. The coefficients A and B are then linear functions of the macroscopic strain components, D_{11} and D_{33} , and B_{2i} . It may also be noted that the field \mathbf{v}^B corresponds to the coefficient C_{22} in the Lee-Mear decomposition. The choice of the expansion field is a generalization of the fields used in the earlier works of Gologanu et al. [23,24] (B_{00} and B_{22}) and Garajeu [27] (B_{00} and B_{20}), which were found to give acceptable results for the yield criterion in the case of the isotropic matrix. Recent work by Monchiet et al. [3] using the Hill matrix also considered the fields B_{00} and B_{22} to describe the expansion field. However, we have chosen to follow the extended approach of [25] and, as will be seen later, the resulting criterion and evolution laws show better agreement with simulation results than those proposed by Monchiet et al. Additional arguments in favor of the choice of the velocity fields may be found in [25].

3. Derivation of the Yield Criterion

The essential step in the derivation of the analytical yield criterion is the evaluation of an upperbound for the macroscopic plastic dissipation, $\Pi^+(\mathbf{D})$, using the chosen set of trial velocity fields. Henceforth, we will use the notation $\Pi(\mathbf{D})$ to refer to the upperbound, for convenience. Using equations (2.9) and (2.7), we have for the RVE of interest

$$\Pi(\mathbf{D}) = \inf_{\mathbf{d} \in \mathcal{K}(\mathbf{D})} \langle \pi(\mathbf{d}) \rangle_{\Omega} = \frac{\sigma_1}{\Omega} \int_{\lambda_1}^{\lambda_2} \int_0^{\pi} \int_0^{2\pi} d_{eq} b L_{\lambda}^2 \sin \beta d\varphi d\beta d\lambda \quad (3.18)$$

where d_{eq} is given by

$$d_{eq}^2 \equiv \frac{2}{3} \mathbf{d} : \hat{\mathbf{h}} : \mathbf{d} \quad (3.19)$$

Note that we no longer need to evaluate the infimum in equation (3.18) since the coefficients of the chosen velocity fields are fixed independently as explained in the

previous section. Using equation (3.16) in (3.19), we have

$$d_{eq}^2 = A^2 d_{eq}^{A^2} + B^2 d_{eq}^{B^2} + \frac{4}{3} AB \mathbf{d}^A : \hat{\mathbf{h}} : \mathbf{d}^B \quad (3.20)$$

where d_{eq}^A and d_{eq}^B are defined similar to d_{eq} in (3.19). Using equation (3.17) along with the incompressibility of \mathbf{d}^A , the above simplifies to

$$d_{eq}^2 = A^2 d_{eq}^{A^2} + 2hABd_{33}^A + hB^2, \quad h \equiv \frac{\hat{h}_{11} + \hat{h}_{22} + 4\hat{h}_{33} - 4\hat{h}_{23} - 4\hat{h}_{31} + 2\hat{h}_{12}}{6} \quad (3.21)$$

where \hat{h}_{ij} represent the components of the symmetric 6×6 matrix (Voigt) representation of the fourth order tensor $\hat{\mathbf{h}}$ in the frame $(\mathbf{e}_1, \mathbf{e}_2, \mathbf{e}_3)$ of figure 3. It is straightforward to demonstrate that the parameter h is invariant with respect to arbitrary coordinate rotations about the void axis, \mathbf{e}_3 . Also note that d_{eq} is, in general, a function of λ, β and φ , even though only axisymmetric velocity fields are used, since d_{eq}^A depends on the orthotropy coefficients which are different in the three coordinate directions.

Expressing the macroscopic deformation rate in terms of the contributions from fields \mathbf{v}^A and \mathbf{v}^B , we have

$$\begin{aligned} D_{11} = D_{22} &= AD_{11}^A + BD_{11}^B = A [c^3/(a_2 b_2^2) - 3c^2 F_2(\lambda_2)/(a_2 b_2)] - B/2 \\ D_{33} &= AD_{33}^A + BD_{33}^B = A [c^3/(a_2 b_2^2) + 6c^2 F_2(\lambda_2)/(a_2 b_2)] + B \end{aligned} \quad (3.22)$$

where equation (3.13)₁ has been used for D_{11}^A and D_{33}^A . The macroscopic stress components are obtained as derivatives of $\Pi(\mathbf{D})$ with respect to the components of the macroscopic deformation rate, by equation (2.12). Using the chain rule, we have

$$\frac{\partial \Pi}{\partial A} = \frac{\partial \Pi}{\partial D_{11}} \frac{\partial D_{11}}{\partial A} + \frac{\partial \Pi}{\partial D_{22}} \frac{\partial D_{22}}{\partial A} + \frac{\partial \Pi}{\partial D_{33}} \frac{\partial D_{33}}{\partial A} = 2D_{11}^A \Sigma_{11} + 2D_{33}^A \Sigma_{33} \quad (3.23)$$

Defining the parameter α_2 by

$$\alpha_2 \equiv \frac{D_{11}^A}{2D_{11}^A + D_{33}^A} = \frac{1}{2} - \frac{b_2}{c} F_2(\lambda_2) \quad (3.24)$$

equation (3.23) becomes

$$\frac{\partial \Pi}{\partial A} = \frac{3c^3}{a_2 b_2^2} \Sigma_h, \quad \Sigma_h \equiv 2\alpha_2 \Sigma_{11} + (1 - 2\alpha_2) \Sigma_{33} \quad (3.25)$$

Using a similar procedure we also obtain

$$\frac{\partial \Pi}{\partial B} = 2D_{11}^B \Sigma_{11} + 2D_{33}^B \Sigma_{33} = \Sigma_{33} - \Sigma_{11} \quad (3.26)$$

Equations (3.25) and (3.26) represent the parametric equation of the macroscopic yield locus, where the ratio A/B acts as the parameter. Elimination of the parameter between the two equations would result in the explicit equation of the yield locus. This proves to be a challenging task, since it requires the explicit evaluation of $\Pi(\mathbf{D})$, given by equation (3.18), and is in fact not feasible analytically. The approach followed in [25] was to introduce a series of approximations that reduce the plastic dissipation integral (3.18) to a form similar to that obtained by Gurson [15], so that the final criterion reduces to the Gurson criterion in the isotropic case. We follow a similar approach and introduce two approximations, designated \mathcal{A}_1 and \mathcal{A}_1 , as explained below. It may be noted that approximation \mathcal{A}_2 is identical to that in [25] while \mathcal{A}_1 differs.

Approximation \mathcal{A}_1 : In equation (3.18), d_{eq} is replaced by its root mean square value obtained by evaluating the integral over the coordinates β and φ , designated d_{eq}^{rms} , as shown below.

$$\Pi(\mathbf{D}) = \frac{\sigma_1}{a_2 b_2^2} \int_{\lambda_1}^{\lambda_2} d_{eq}^{rms} b(2a^2 + b^2) d\lambda \quad (3.27)$$

where

$$d_{eq}^{rms} = \left[\frac{3}{4\pi(2a^2 + b^2)} \int_0^\pi \int_0^{2\pi} d_{eq}^2 L_\lambda^2 \sin \beta d\varphi d\beta \right]^{1/2} \quad (3.28)$$

and we have used the expression for the volume of the RVE, given by $\Omega = 4\pi a_2 b_2^2/3$ to obtain the simplified form (3.27). This approximation is necessary since the triple integral in (3.18) can not be evaluated in closed form, whereas d_{eq}^{rms} can be evaluated using equation (3.28). Note that this approximation preserves the upper bound character of the approach since the RMS value is always greater than the mean. d_{eq}^{rms} is a function of λ alone, and using a change of variable $x \equiv c^3/ab^2$, equation (3.27) can be written in the simple form

$$\Pi(\mathbf{D}) = \sigma_1 x_2 \int_{x_2}^{x_1} d_{eq}^{rms} \frac{dx}{x^2} \quad (3.29)$$

where d_{eq}^{rms} has the form

$$d_{eq}^{rms} = \sqrt{A^2 P(x) + hB^2 + 2hABQ(x)} \quad (3.30)$$

The functions $P(x)$ and $Q(x)$ above are the mean values, obtained using equation (3.28), of the d_{eq}^A and d_{33}^A terms appearing in the expansion for d_{eq}^2 , equation (3.21). These functions have complicated expressions and are evaluated using MAPLE software. However, despite their lengthy expressions, they have a relatively simple behavior in the domain of interest, as indicated by their limiting values for the cases of $x \rightarrow 0$ (spherical void) and $x \rightarrow \infty$ (cylindrical void for the prolate case and a ‘‘sandwich’’ in the oblate case). The limiting values of $P(x)$ are

$$P(x \rightarrow 0) = \frac{4}{5}(h + 2h_t + 2h_a)x^2 \quad (3.31)$$

$$P(x \rightarrow \infty) = \begin{cases} 3h_t x^2 & \text{(p)} \\ 9h(3\pi B_{22} + 4B_{21})^2 + 6h_a(\pi B_{21} + 12B_{22})^2 & \text{(o)} \end{cases} \quad (3.32)$$

where the parameter h was introduced earlier, in equation (3.21), and h_t and h_a are given by

$$h_t \equiv \frac{\hat{h}_{11} + \hat{h}_{22} + 2\hat{h}_{66} - 2\hat{h}_{12}}{4}, \quad h_a \equiv \frac{\hat{h}_{44} + \hat{h}_{55}}{2} \quad (3.33)$$

with \hat{h}_{ij} as the components of the tensor $\hat{\mathbf{h}}$ expressed in Voigt form, in the frame $(\mathbf{e}_1, \mathbf{e}_2, \mathbf{e}_3)$ associated with the RVE of figure 3. It can be shown that, similar to the case of h , the values of h_t and h_a are invariant with respect to arbitrary coordinate rotations about the symmetry axis of the RVE, \mathbf{e}_3 . Notice that in the prolate case, $P(x)$ may be considered to be approximately proportional to x^2 in both limits, whereas in the oblate case, $P(x)$ tends to a constant value in the limit of $x \rightarrow \infty$. Figure 5 shows the variation of $P(x)/x^2$ as a function of e , the eccentricity of the current spheroid, for the case of prolate cavities and three different sets of material anisotropy parameters, corresponding to an isotropic matrix, Material 1 and Material 2 from Table 1 on page 49. In all cases, the material's \mathbf{e}_3 -axis of orthotropy is aligned with the void axis. The independent variable has been changed to e , so that the entire domain of variation of the function can be shown. The variable x and e are related by $x = e^3/(1 - e^2)^n$, where $n = 1$ for prolate cavities and $n = 1/2$ for oblate cavities.

The function $Q(x)$, on the other hand, is independent of the material anisotropy parameters. It is seen that $Q(x)$ can be considered approximately proportional to x for prolate cavities and constant for oblate cavities. The values of $Q(x)$ in the limiting cases are shown below.

$$\lim_{x \rightarrow 0} \frac{Q(x)}{x} = \lim_{x \rightarrow \infty} \frac{Q(x)}{x} = 0 \quad (\text{p}) \quad (3.34)$$

$$\begin{cases} \lim_{x \rightarrow 0} Q(x) = 0 \\ \lim_{x \rightarrow \infty} Q(x) = 12B_{21} + 9\pi B_{22} \end{cases} \quad (\text{o}) \quad (3.35)$$

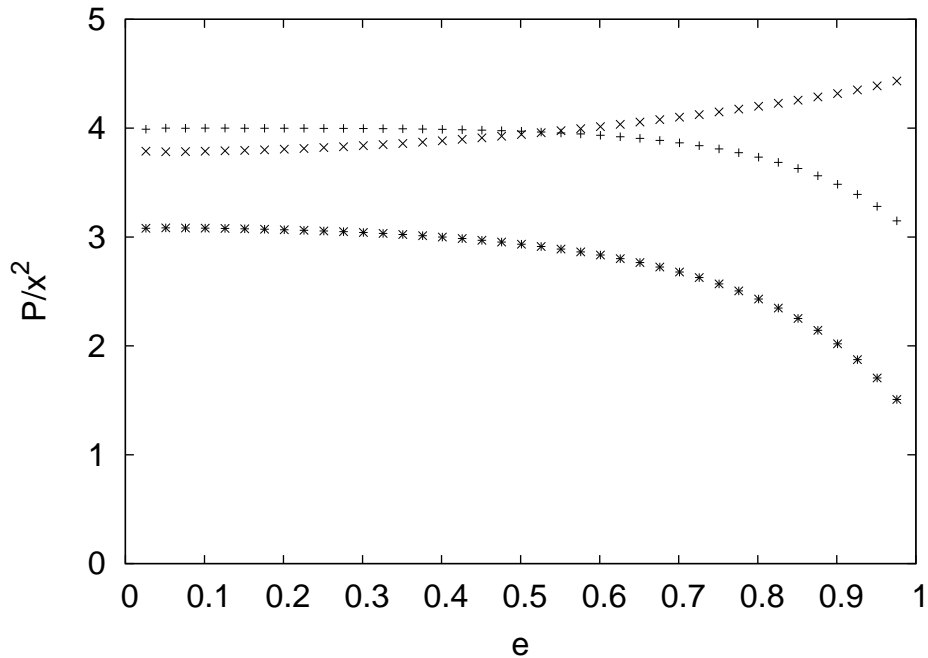


Fig. 5. Variation of P/x^2 as a function of the eccentricity of the current spheroid e for an isotropic matrix (symbol +), Material 1 (symbol \times) and Material 2 (symbol $*$) from Table 1. In all cases B_{20} and B_{21} were taken as zero.

The variation of $Q(x)/x$ as a function of the eccentricity of the current spheroid, e , is shown in figure 6 for prolate cavities.

Based on the above observations, we see that $P(x)$ varies like x^2 and $Q(x)$ like x through the domain of interest for prolate cavities, but not for oblate cavities. However, introducing the change of variable proposed by Gologanu et al. [24,25] and writing $P(x) = F(u)u^2$, where $u \equiv x$ for prolate cavities and $u \equiv x/(1+x)$ for oblate cavities, we may consider the function $F(u)$ to be approximately constant in the domain $x \in (0, \infty)$ for both prolate and oblate cavities. Also, following Gologanu et al. [25], we write $Q(x) = F(u)G(u)u^2$. Substituting for $P(x)$ and $Q(x)$, as above, in the expression for d_{eq}^{rms} (3.30), the plastic dissipation integral, equation (3.29), can

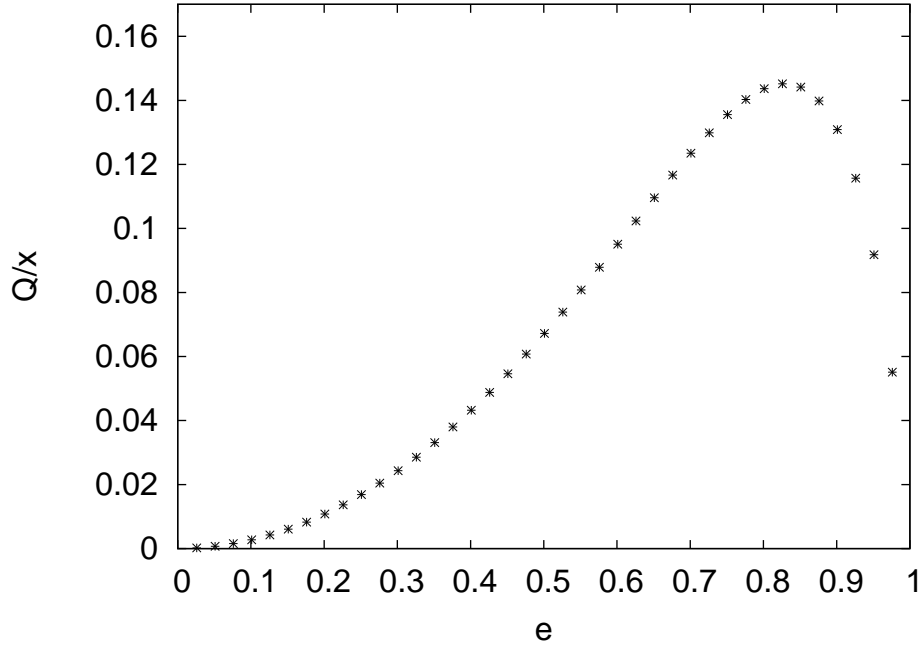


Fig. 6. Variation of Q/x as a function of the eccentricity of the current spheroid e . In all cases B_{20} and B_{21} were taken as zero.

be written

$$\Pi(\mathbf{D}) = \sigma_1 x_2 \int_{u_2}^{u_1} \sqrt{[AF(u) + hBG(u)]^2 u^2 + B^2 H^2(u)} \frac{du}{u^2} \quad (3.36)$$

where $H(u) \equiv \sqrt{h(1 - hG^2(u)u^2)}$. With these changes, we now introduce the next approximation.

Approximation \mathcal{A}_2 : In equation (3.36), the functions $F(u)$, $G(u)$ and $H(u)$ are replaced by constants, designated \bar{F} , \bar{G} and \bar{H} , respectively.

This approximation is identical to the one that was used by Gologanu et al. in the case of spheroidal voids and the isotropic matrix [25]. Note that although this approximation is justified in the case of function $F(u)$, the same can not be said for functions $G(u)$ and $H(u)$, since these functions tend to infinity in the limit of spherical cavities. However, this approximation was found to give good results in the case of

the isotropic matrix. Also, the functions $G(u)$ and $H(u)$ result from the “crossed” term in the expression for d_{eq}^{rms} (3.30) and good estimates of the yield criterion were obtained in the case of the isotropic matrix by Gologanu et al. [23] and Garajeu [27] by completely neglecting this term. Therefore, the effect of the “crossed” term on the yield criterion is expected to be “weak” in which case replacing these functions by constants is a reasonable approximation. In spite of the above approximation, the final criterion does reduce to the Gurson [15] criterion in the limit of spherical cavities and the isotropic matrix, as will be seen later.

With these changes, the integral for the plastic dissipation can be written in the form

$$\Pi(\mathbf{D}) = \sigma_1 x_2 \int_{u_2}^{u_1} \sqrt{A'^2 u^2 + B'^2} \frac{du}{u^2}, \quad A' \equiv \bar{F}A + h\bar{G}B, \quad B' \equiv \bar{H}B \quad (3.37)$$

Indeed the object of approximation \mathcal{A}_2 was to recover the above form for the plastic dissipation integral, which is similar to the form obtained by Gurson [15]. This has the advantage that the final criterion will have a form similar to that of Gurson and will reduce to it as a special case, which is desirable since the Gurson model is known to be a tight upper bound for the actual yield criterion in the isotropic case.

From this point, the calculations are formally identical to those in [25]. Evaluation of the derivatives $\partial\Pi/\partial A'$ and $\partial\Pi/\partial B'$ and elimination of the ratio A'/B' between the two equations results in

$$\frac{1}{\sigma_1^2} \left(\frac{\partial\Pi}{\partial B'} \right)^2 + 2(g+1)(g+f) \cosh \frac{1}{\sigma_1 x_2} \frac{\partial\Pi}{\partial A'} - (g+1)^2 - (g+f)^2 \quad (3.38)$$

where the parameter g is taken as zero for prolate cavities and x_2 for oblate cavities. Expressing $\partial\Pi/\partial A'$ and $\partial\Pi/\partial B'$ in terms of $\partial\Pi/\partial A$ and $\partial\Pi/\partial B$ using equations (3.37)_{2,3} and then in terms of the macroscopic stress components using equations (3.25) and (3.26), we obtain the final expression for the yield criterion, which is in

fact formally identical to that obtained by Gologanu et al. [25].

$$\frac{C}{\sigma_1^2}(\Sigma_{33} - \Sigma_{11} + \eta\Sigma_h)^2 + 2(g+1)(g+f) \cosh \kappa \frac{\Sigma_h}{\sigma_1} - (g+1)^2 - (g+f)^2 = 0 \quad (3.39)$$

where,

$$C \equiv \frac{1}{H^2}, \quad \eta \equiv -3x_2 \frac{h\bar{G}}{\bar{F}}, \quad \kappa \equiv \frac{3}{\bar{F}}, \quad g \equiv \begin{cases} 0 & \text{(p)} \\ x_2 & \text{(o)} \end{cases} \quad (3.40)$$

Note that although the form of the criterion is identical to that in [25], the parameters κ , α_2 , C and η are now functions of the anisotropy parameters h , h_t and h_a in addition to the porosity, f , and void shape parameter, S . Their expressions are determined in the following section.

4. Determination of the Criterion Parameters

We follow an approach essentially similar to that of Gologanu et.al [25] in order to determine the closed form expressions for the criterion parameters, κ , α_2 , C and η , which involves further approximations. The main consideration determining the nature of these approximations is that the resulting yield locus is close to the “exact” yield locus, determined numerically in chapter IV.

a. Parameters κ and α_2

The parameters κ and α_2 , defined by equations (3.40)₃ and (3.24) respectively, depend on the components of the “expansion” field, identified by the parameters B_{2i} . Recall that these parameters were left undefined thus far in the derivations. The parameter κ is tied to the definition of the constant \bar{F} . \bar{F} is chosen such that replacement of \bar{F} for $F(u)$ in equation (3.36) results in the exact value of the integral in the case of

purely hydrostatic loading and assuming $B = 0$. In such case, \bar{F} is given by

$$\bar{F} = \left(\ln \frac{u_1}{u_2} \right)^{-1} \int_{u_2}^{u_1} F(u) \frac{du}{u} \quad (3.41)$$

and since the right hand side, which is proportional to the plastic dissipation, depends on the parameters B_{2i} , the best choice of \bar{F} that gives the closest fit to the true yield locus will be obtained by minimizing the above integral with respect to these parameters. However, this minimization is not tractable analytically, but may be performed numerically for specific choices of the limits u_1 and u_2 (corresponding to specific values of f and S). In order to obtain a closed form expression for \bar{F} for general values of f and S , the following scheme is used, which is a variant of the method used in [25].

First, the parameters B_{2i} are taken to be functions of u , rather than constants. Their values are obtained by minimizing an approximation to the function $d_{eq}^{A^2}$, obtained by replacing the variable $\cos^2 \beta$ that appears in the expansion of $d_{eq}^{A^2}$ by $1/3$, with respect to the unknown parameters B_{2i} . This was the method used in [25] to obtain the values of B_{2i} , but they also used this method to approximate the value of $\Pi(\mathbf{D})$, which we no longer do here due to poor results obtained for the case of anisotropic matrix. Note that the existence and uniqueness of the above minimum is guaranteed, since $d_{eq}^{A^2}$ is a positive definite quadratic form in the values of B_{2i} . The minimization is performed while respecting the linear constraints among the parameters, B_{2i} , equation (3.15), imposed by the homogeneous deformation rate boundary conditions. The resulting values of B_{2i} are functions of u and the anisotropy factors, h, h_t and h_a . However, we choose to ignore the dependence on the anisotropy factors and use the isotropic values of $h = h_t = h_a = 1$, so that B_{2i} are functions of u alone. Note that, *a priori*, one would expect the microscopic velocity field, and hence B_{2i} , to depend on material anisotropy. Indeed, this is verified to be the case in our numerical

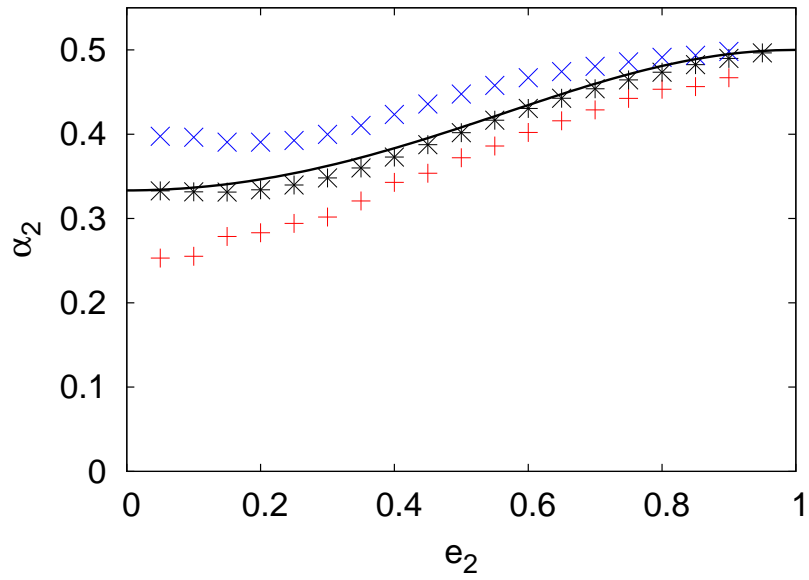
results to be presented in chapter IV, and in figure 7 for the parameter α_2 . However, our numerical experience indicates that using the values of B_{2i} as functions of h, h_t and h_a , obtained above, grossly over-predicts this effect and a better yield criterion is obtained by constraining B_{2i} to not depend on the anisotropy parameters. Note that \bar{F} and κ will still depend on the anisotropy factors, since the expression for $F(u)$ depends explicitly on h, h_t and h_a .

Once the values of B_{2i} are specified, the microscopic deformation field is completely defined and one can calculate the expression for the parameter α_2 given by (3.24). This yields

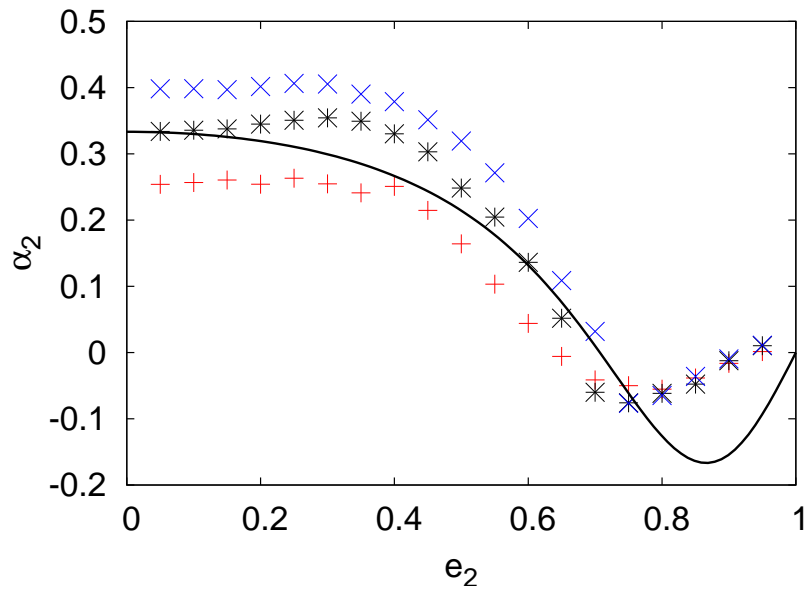
$$\alpha_2 = \begin{cases} \frac{(1 + e_2^2)}{(1 + e_2^2)^2 + 2(1 - e_2^2)} & \text{(p)} \\ \frac{(1 - e_2^2)(1 - 2e_2^2)}{(1 - 2e_2^2)^2 + 2(1 - e_2^2)} & \text{(o)} \end{cases} \quad (3.42)$$

where e_2 denotes the eccentricity of the RVE and hence depends implicitly on f and S . Note that these expressions of α_2 are identical to those obtained by [25] for the isotropic case, which is a consequence of the fact that we have neglected the dependence of B_{2i} on anisotropy. Figure 7 shows the variation of α_2 as a function of e_2 for prolate and oblate RVEs. Numerically determined values of α_2 using the method explained in chapter IV for RVEs of porosity, $f = 0.01$, and three different material anisotropy parameters are also shown using discrete points. The anisotropy factors were so chosen as to obtain the largest possible range of α_2 in figure 7. Notice that the assumption that α_2 is independent of the anisotropy parameters is not strictly true, but the effect appears to be weak for both prolate and oblate cavities. On the other hand numerical curves of α_2 , obtained for different values of f (not shown here), indicates that the dependence of α_2 on f is weak, apart from the implicit dependence through e_2 .

For the case of prolate cavities, it turns out that the function $F(u)$ obtained by us-



(a)



(b)

Fig. 7. Variation of α_2 as a function of e_2 for (a) prolate and (b) oblate RVEs, with $f = 0.01$. Discrete points correspond to numerically determined values of α_2 for isotropic matrix (*), Material 1 (+) and Material 2 (\times) from Table 1.

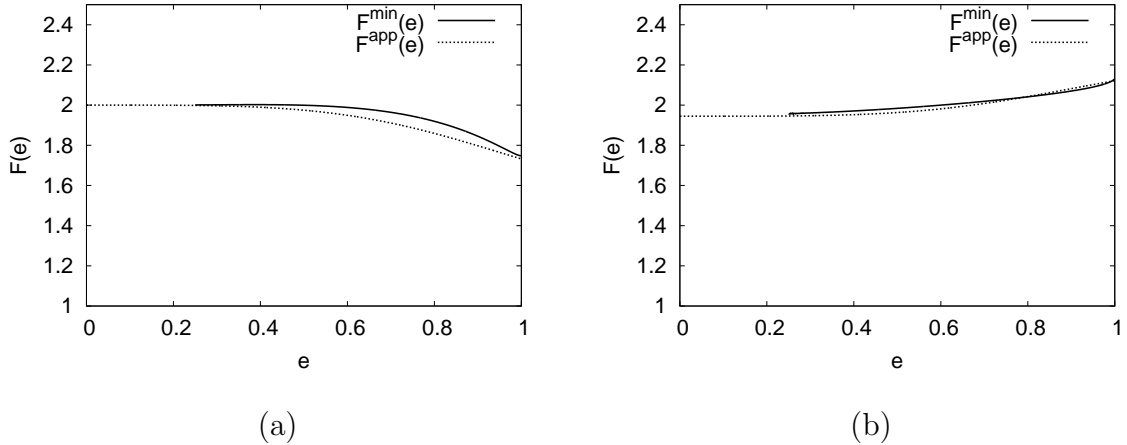


Fig. 8. Variation of $F(e)$ as a function of e for prolate RVEs, with $f = 0.001$ and $w_1 = 5$ (a) Isotropic matrix (b) Material 1 from Table 1.

ing the above determined values of B_{2i} , designated $F^{app}(u)$, results in close agreement with the true function $F(u)$ that minimizes the integral of equation (3.41), regardless of the values of u_1 and u_2 and for all values of material anisotropy parameters tested. However, this function is still too complicated to be used in equation (3.41) to find \bar{F} . It may be observed that $F^{app}(u)$ has the form $F^{app}(u) = \sqrt{hF_1 + h_tF_2 + h_aF_3}$, where the functions F_1, F_2 and F_3 depend on u alone. Despite their complicated expression, these functions can be well approximated by fits of the form $C_1 \frac{(1-e^4)}{(3+e^4)^2} + C_2$, where the eccentricity of the current spheroid, e , is used as the independent variable and the constants C_1 and C_2 are determined by fitting the original function at the end points, i.e. $e = 0$ and $e = 1$. This results in the following expression for $F^{app}(e)$

$$F^{app}(e) = \sqrt{\frac{9}{5}(4h + 8h_a - 7h_t) \frac{(1 - e^4)}{(3 + e^4)^2} + 3h_t} \quad (p) \quad (3.43)$$

The figure 8 compares $F^{app}(e)$ with the true function that minimizes the integral in (3.41), designated $F^{min}(e)$ for two different material anisotropy parameters and for $f = 0.001$ and the void aspect ratio, $w_1 = 5$.

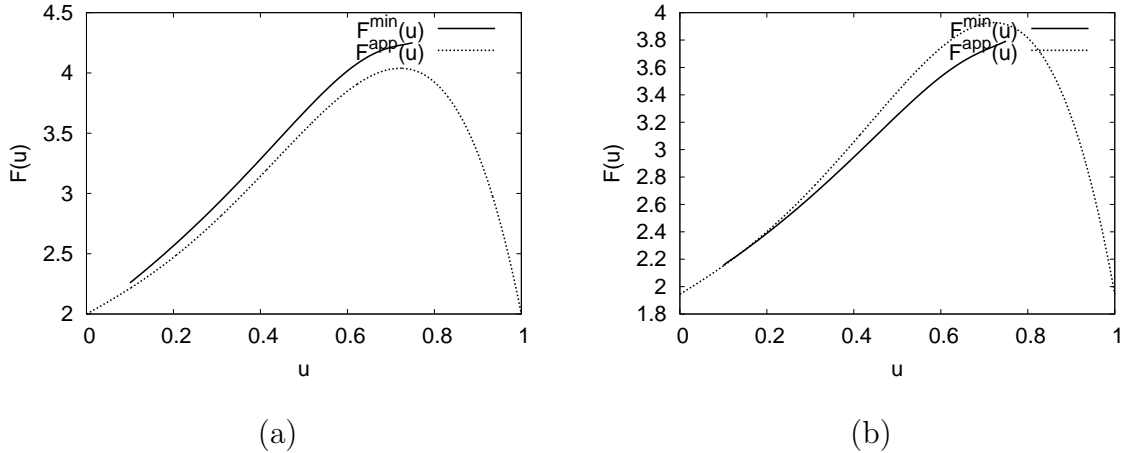


Fig. 9. Variation of $F(u)$ as a function of u for oblate RVEs, with $f = 0.001$ and $w_1 = 1/5$ (a) Isotropic matrix (b) Material 1 from Table 1.

However, in the case of oblate cavities the above approach does not result in a satisfactory approximation for $F^{min}(u)$. Therefore, we use a heuristic modification of the function $F^{app}(u)$ proposed by Gologanu et al. [25] and given below

$$F^{app}(u) = \sqrt{\frac{4}{5}(h + 2h_a + 2h_t)(1 + u + 2u^{5/2} - 3u^5)} \quad (o) \quad (3.44)$$

This function gives an acceptable agreement with the true function that minimizes the integral (3.41), determined numerically, as illustrated in figure 9 for two different material anisotropy parameters and $f = 0.001$ and $w_1 = 1/5$.

The parameter κ can be determined by substituting (3.43) and (3.44) in (3.41) and then using equation (3.40)₃. For the prolate case, since the integral cannot be evaluated in closed form, the mean of $F^{app^2}(e)$ is evaluated using equation (3.41) and the square root of this value is assigned to \bar{F} . It is verified numerically that for all

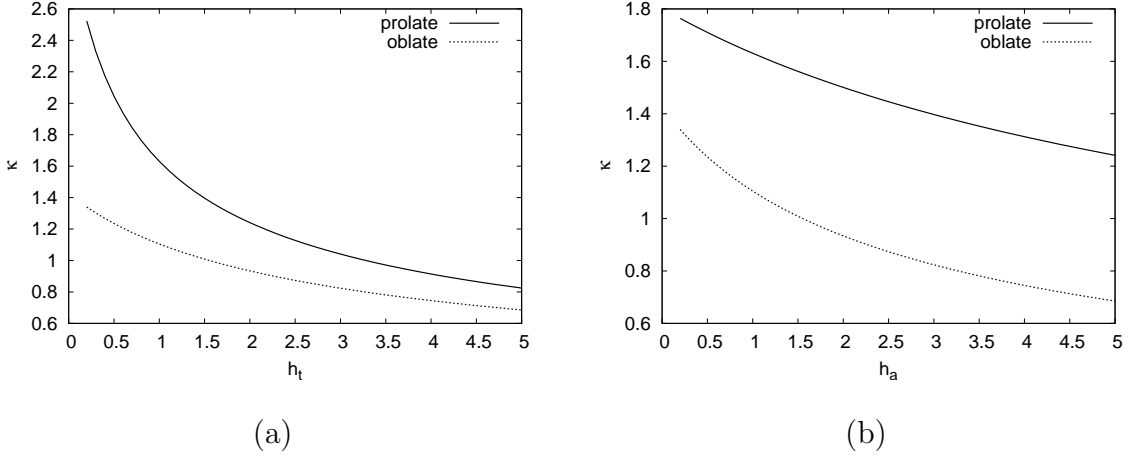


Fig. 10. (a) Variation of κ with h_t for $h = h_a = 1.0$. (b) Variation of κ with h_a for $h = h_t = 1.0$. In both cases, $f = 0.01$ and $w = 5$ (prolate) and $1/5$ (oblate).

values of e_1 and e_2 , the two values are close to each other. Thus

$$\kappa = \begin{cases} \sqrt{3} \left\{ \frac{1}{\ln f} \left[\frac{2}{3} \ln \frac{1-e_2^2}{1-e_1^2} + \frac{3+e_2^2}{3+e_2^4} - \frac{3+e_1^2}{3+e_1^4} + \frac{1}{\sqrt{3}} \left(\tan^{-1} \frac{e_2^2}{\sqrt{3}} - \tan^{-1} \frac{e_1^2}{\sqrt{3}} \right) \right. \right. & \text{(p)} \\ \left. \left. - \frac{1}{2} \ln \frac{3+e_2^4}{3+e_1^4} \right] \frac{4h+8h_a-7h_t}{10} + \frac{4(h+2h_a+2h_t)}{15} \right\}^{-1/2} & \text{(3.45)} \\ \frac{3}{2} \left(\frac{h+2h_a+2h_t}{5} \right)^{-1/2} \left\{ 1 + \frac{(g_f-g_1) + \frac{4}{5}(g_f^{5/2}-g_1^{5/2}) - \frac{3}{5}(g_f^5-g_1^5)}{\ln \frac{g_f}{g_1}} \right\}^{-1} & \text{(o)} \end{cases}$$

where

$$g_f \equiv \frac{g}{g+f}, \quad g_1 \equiv \frac{g}{g+1} \quad (3.46)$$

In the case of spherical voids, (3.45) reduces to $\kappa = 3/2\sqrt{5/(h+2h_a+2h_t)}$ and in the limit of cylindrical voids $\kappa = \sqrt{3/h_t}$, which are results established in [22]. Figure 10 shows the variation of κ with the anisotropy parameters h_t and h_a , for prolate and oblate cavities with $f = 0.01$ and $w_1 = 5$ and $1/5$ respectively.

b. Parameters C and η

The parameters C and η are tied to the constants \bar{G} and \bar{H} by equations (3.40)_{1,2}. These are now determined by forcing the approximate analytical yield locus to pass

through and be tangent to known exact points on the two field yield locus (i.e. the yield locus defined by equations (3.25) and (3.26) without the approximations \mathcal{A}_1 and \mathcal{A}_2), which can be determined in the case of $A = 0$. In this case, the derivatives of the plastic dissipation, $\partial\Pi/\partial A$ and $\partial\Pi/\partial B$ can be evaluated exactly and then using equations (3.25) and (3.26), we obtain

$$\begin{aligned}\Sigma_h/\sigma_1 &= \pm 2\sqrt{h}(\alpha_2 - \alpha_1) \\ (\Sigma_{33} - \Sigma_{11})/\sigma_1 &= \pm\sqrt{h}(1 - f)\end{aligned}\tag{3.47}$$

where the parameter α_1 is defined in a manner similar to α_2 (3.24), by

$$\alpha_1 \equiv \frac{D_{11}^{vA}}{2D_{11}^{vA} + D_{33}^{vA}}\tag{3.48}$$

In the above equation, \mathbf{D}^{vA} is the ‘‘macroscopic deformation rate of the void’’ due to the field A , defined by

$$\mathbf{D}^{vA} \equiv \langle \mathbf{d}^A \rangle_\omega = \frac{3}{4\pi a_1 b_1^2} \int_{\partial\omega} \frac{1}{2} (\mathbf{v} \otimes \mathbf{n} + \mathbf{n} \otimes \mathbf{v}) dS\tag{3.49}$$

The surface integral form of \mathbf{D}^{vA} , above, is obtained by using the divergence theorem.

The two algebraic equations that result from substituting (3.47) in (3.39) and equating the slopes of the analytical and the exact two field yield loci at these points, can be solved for the values of the two unknown parameters C and η . This results in the following expressions

$$\eta = -\frac{\kappa Q^*(g+1)(g+f)\text{sh}}{(g+1)^2 + (g+f)^2 + (g+1)(g+f)[\kappa H^*\text{sh} - 2\text{ch}]},\tag{3.50}$$

$$C = -\frac{\kappa(g+1)(g+f)\text{sh}}{(Q^* + \eta H^*)\eta}, \quad \text{sh} \equiv \sinh(\kappa H^*), \quad \text{ch} \equiv \cosh(\kappa H^*)$$

where $H^* \equiv \Sigma_h/\sigma_1$ and $Q^* \equiv (\Sigma_{33} - \Sigma_{11})/\sigma_1$ from (3.47). Note that the above expressions are formally identical to those in [25], except that the parameters H^* and

Q^* now depend on the anisotropy factor, h , by (3.47).

The expression for α_1 is determined in a manner identical to that in [25]. Similar to the case of α_2 , which was found to be closely approximated by a function of e_2 alone, it is assumed that α_1 depends only on e_1 (or S) and is independent of f and the anisotropy parameters. In such case, the value of α_1 can be evaluated by letting the boundary of the RVE tend to infinity (i.e. $a_2, b_2 \rightarrow \infty$ or $f \rightarrow 0$). In such case, it turns out that one must take $B_{20} = B_{21} = 0$ for the velocity fields to not diverge. The remaining parameter B_{22} is then fixed by the boundary conditions and the integrals (3.49) can be evaluated in closed form. Using equation (3.48), we obtain

$$\alpha_1 = \begin{cases} [e_1 - (1 - e_1^2) \tanh^{-1} e_1] / (2e_1^3) & \text{(p)} \\ [-e_1(1 - e_1^2) + \sqrt{1 - e_1^2} \sin^{-1} e_1] / (2e_1^3) & \text{(o)} \end{cases} \quad (3.51)$$

which are identical to the expressions from [25].

5. Special Cases

Equation (3.39) provides the homogenized yield criterion for plastically anisotropic materials containing spheroidal voids. The parameters in the criterion, $\kappa, \alpha_2, C, \eta$ and α_1 are defined by equations (3.45), (3.42), (3.50)_{1,2} and (3.51) respectively, in terms of the microstructural parameters, f and S , and the anisotropy parameters h, h_t and h_a . By considering the special cases of an isotropic matrix and/or spherical or cylindrical voids, many of the existing results can be recovered, as shown below.

In the case of spheroidal voids in an isotropic matrix, i.e. $h = h_t = h_a = 1$, the criterion established by Gologanu et al. [25] is recovered exactly in the case of oblate cavities. However, in the case of prolate cavities the two criteria differ in the exponential ‘‘cosh’’ term of the criterion, equation (3.39). This difference is due to the fact that we have used a different approach to defining the constant \bar{F} which is

tied to the value of κ . The approximate method of Gologanu et al. [25] for defining the variable κ gave good results for the isotropic matrix, but was found to give poor results in the case of anisotropic matrix properties. In the isotropic case, it can be verified that although the expression for κ differs, the two yield criteria are very close to each other for most practical values of f and S .

Other special cases to be considered are the two limiting configurations of spheroidal cavities, namely spherical voids and infinitely long cylindrical holes. For these two void geometries in an orthotropic matrix, closed form yield criteria were established by Benzerga and Besson [1, 22]. In the case of spherical or cylindrical cavities in an orthotropic matrix, equation (3.39) reduces to

$$\frac{(\Sigma_{33} - \Sigma_{11})^2}{h\sigma_1^2} + 2f \cosh \kappa \frac{\Sigma_m}{\sigma_1} - 1 - f^2 = 0 \quad (3.52)$$

where,

$$\kappa = \begin{cases} \frac{3}{2} \sqrt{\frac{5}{h+2h_a+2h_t}} & \text{(sphere)} \\ \sqrt{\frac{3}{h_t}} & \text{(cylinder)} \end{cases} \quad (3.53)$$

The value of κ in both the limits above agrees with that established in [22]. In the case of axisymmetric loadings, the coefficient of the square term, $(\Sigma_{33} - \Sigma_{11})^2$, in [22] was $(h_{11} + h_{22} + 4h_{33} - 4h_{23} - 4h_{31} + 2h_{12})/6$, where h_{ij} are the components (in Voigt form) of \mathbf{h} , the Hill anisotropy tensor, introduced in chapter II. In general, this is not equal to $1/h$ as in equation (3.52). However, a simple analysis using the definitions of the components of the \mathbf{h} and $\hat{\mathbf{h}}$ tensors in terms of the five strain ratios of the material, provided in Appendix A, shows that the value of the above coefficient is close to $1/h$, and reduces to it in the case of transverse isotropy in the plane normal to the void axis. In the general case of orthotropy it may be verified that, assuming one of the directions of material orthotropy coincides with the void axis, the difference of the two coefficients is proportional to the square of the difference of the strain ratios

in the other two directions of material orthotropy, which may be expected to be small for most materials.

In the case of spherical or cylindrical cavities in an isotropic matrix, we have $h = h_t = h_a = 1$ and $\kappa = 3/2$ for spherical cavities and $\sqrt{3}$ for cylindrical cavities. In these cases, equation (3.52) reduces to Gurson's original results [14, 15].

CHAPTER IV

NUMERICAL DETERMINATION OF THE EXACT YIELD CRITERION

In order to validate the analytical yield criterion derived in the previous chapter, we now develop a numerical scheme to derive the “exact” yield criterion for specific values of porosity, f , and the void shape parameter, S , representing a given microstructure. To illustrate the principle used in determining the numerical yield locus, we refer back to the original definition of the macroscopic yield locus, defined as the envelope of the hyperplanes in stress space given by

$$\boldsymbol{\Sigma} : \mathbf{D} = \Pi(\mathbf{D}) \quad (4.1)$$

where the components of \mathbf{D} act as the parameters (see discussion in chapter II, page 14), and $\Pi(\mathbf{D})$ is defined by equation (2.9). In the case of axisymmetric loadings assumed in the derivations in chapter III, the macroscopic yield locus is a function of the two independent macroscopic stress components, see equation (3.39), and hence can be represented in a plane. By convention, and for comparison to the yield loci available elsewhere in the literature for porous materials, the yield loci are represented here in a plane with the mean macroscopic stress, $\Sigma_m = \Sigma_{kk}/3$, as the abscissa and the macroscopic effective stress, $\Sigma_e \equiv \sqrt{\frac{3}{2}\boldsymbol{\Sigma}' : \boldsymbol{\Sigma}'}$ ($= \Sigma_{33} - \Sigma_{11}$ for axisymmetric loadings), as the ordinate. The ratio of the mean stress to the effective stress is known as the stress triaxiality ratio, $T \equiv \Sigma_m/\Sigma_e$, which corresponds to a radial line in the $\Sigma_m - \Sigma_e$ plane. It is related to the ratio of the normal stress components through

$$X \equiv \frac{\Sigma_{33}}{\Sigma_{11}} = \frac{9T}{3T - 1} - 2 \quad (4.2)$$

for axisymmetric loading paths. To find the intersection of the above radial line with the yield locus, we use equation (4.1) to write

$$\Sigma_{11} = \frac{\Pi(D_{11}, D_{33})}{2D_{11} + XD_{33}} \quad (4.3)$$

Noting that since $\Pi(D_{11}, D_{33})$ is a homogeneous function of degree one in the components of \mathbf{D} , the above ratio is homogeneous of degree zero, one may scale the values of D_{11} and D_{33} arbitrarily in evaluating the right hand side of the above equation. For convenience, we impose the constraint that

$$2D_{11} + XD_{33} = 1 \quad (4.4)$$

in which case, equation (4.3) becomes

$$\Sigma_{11} = \Pi(D_{11}, D_{33}) \quad (4.5)$$

where $\Pi(D_{11}, D_{33})$ is obtained by evaluating the infimum in equation (2.9), using a subset of the complete set of axisymmetric velocity fields in the Lee-Mear decomposition, equations (3.8) and (3.9). By varying the value of X , we can then evaluate individual points on the macroscopic yield locus. The above approach may be referred to as numerical limit analysis of the “exact” yield criterion, and was also used by Gologanu et al. in [25]. The phrase “exact” here implies that the yield locus thus obtained is a rigorous upperbound to the true yield locus, that gets closer to the true locus as the number of velocity fields is increased. In practice, it is observed that using a few fields (< 20) corresponding to the lower order Lee-Mear coefficients results in a very good estimate of the yield locus, and addition of further velocity fields (upto 50) does not result in perceptible improvement in the upper bound obtained. The numerical scheme used to minimize the plastic dissipation in equation (4.5) is explained in the following section.

A. Numerical Minimization of the Plastic Dissipation

For a given set of microstructural parameters, f and S , an RVE can be defined (see figure 3) by solving for the eccentricities of the void and the RVE, e_1 and e_2 , from

$$\frac{1}{1 - e_1^2} = e^{2|S|}$$

$$\frac{(1 - e_2^2)^n}{e_2^3} = \frac{1}{f} \frac{(1 - e_1^2)^n}{e_1^3}, \quad n = \begin{cases} 1 & \text{(p)} \\ 1/2 & \text{(o)} \end{cases} \quad (4.6)$$

and the coordinates λ_1 and λ_2 can be determined from the relation $e = 1/\cosh \lambda$. The focal length c can be set arbitrarily since the problem is scale invariant. The plastic dissipation is defined by

$$\Pi(\mathbf{D}) = \inf_{\mathbf{d} \in \mathcal{K}(\mathbf{D})} \langle \pi(\mathbf{d}) \rangle_{\Omega} = \inf_{\mathbf{d} \in \mathcal{K}(\mathbf{D})} \frac{\sigma_1}{\Omega} \int_{\lambda_1}^{\lambda_2} \int_0^{\pi} \int_0^{2\pi} d_{eq} L_{\lambda} L_{\beta} L_{\varphi} d\varphi d\beta d\lambda \quad (4.7)$$

where $d_{eq} = \sqrt{\frac{2}{3} \mathbf{d} : \hat{\mathbf{h}} : \mathbf{d}}$. The infimum is taken over all kinematically admissible deformation fields. For the case of axisymmetric deformations, we have

$$\mathbf{d} = d_{\lambda\lambda} \mathbf{g}^{\lambda} \otimes \mathbf{g}^{\lambda} + d_{\beta\beta} \mathbf{g}^{\beta} \otimes \mathbf{g}^{\beta} + d_{\varphi\varphi} \mathbf{g}^{\varphi} \otimes \mathbf{g}^{\varphi} + d_{\lambda\beta} \mathbf{g}^{\lambda} \otimes \mathbf{g}^{\beta} \quad (4.8)$$

where the components d_{ij} are given by equations (3.5) and (3.6) respectively for prolate and oblate cavities. Introducing an orthonormal basis $(\mathbf{e}_{\lambda}, \mathbf{e}_{\beta}, \mathbf{e}_{\varphi})$, whose vectors are collinear with the vectors $(\mathbf{g}^{\lambda}, \mathbf{g}^{\beta}, \mathbf{g}^{\varphi})$, the above equation becomes

$$\mathbf{d} = \frac{1}{L_{\lambda}^2} (d_{\lambda\lambda} \mathbf{e}_{\lambda} \otimes \mathbf{e}_{\lambda} + d_{\beta\beta} \mathbf{e}_{\beta} \otimes \mathbf{e}_{\beta} + d_{\lambda\beta} \mathbf{e}_{\lambda} \otimes \mathbf{e}_{\beta}) + \frac{1}{L_{\varphi}^2} (d_{\varphi\varphi} \mathbf{e}_{\varphi} \otimes \mathbf{e}_{\varphi}) \quad (4.9)$$

Representing \mathbf{d} as a column vector in Voigt notation, we have

$$[\mathbf{d}] = \begin{bmatrix} \frac{d_{\lambda\lambda}}{L_{\lambda}^2} & \frac{d_{\beta\beta}}{L_{\lambda}^2} & \frac{d_{\varphi\varphi}}{L_{\varphi}^2} & 0 & 0 & \frac{\sqrt{2}d_{\lambda\beta}}{L_{\lambda}^2} \end{bmatrix}^T \quad (4.10)$$

In the Lee-Mear decomposition for \mathbf{v} , equations (3.8) and (3.9), let us adopt velocity fields corresponding to B_{00} , B_{km} and C_{km} , where $k = 2, 4, 6, \dots, K$ and $m = 0, 1, 2, \dots, M$, to evaluate the tensor \mathbf{d} . This corresponds to a total of $N = K(M+1)+1$ velocity fields. From equations (3.5) and (3.6), it is clear that $[\mathbf{d}]$ can be written in the form

$$[\mathbf{d}] = [\mathcal{L}][A] \quad (4.11)$$

where $[\mathcal{L}] = [\mathcal{L}(\lambda, \beta, \varphi)]$ is a $6 \times N$ matrix derived from (3.5) and (3.6) and $[A]$ is an $N \times 1$ column vector given by

$$[A] \equiv [B_{00} \quad [B_{km}]^T \quad [C_{km}]^T]^T \quad (4.12)$$

with $[B_{km}]$ and $[C_{km}]$ defined as column vectors of the chosen Lee-Mear coefficients. The components of the tensor $\hat{\mathbf{h}}$ in the frame $(\mathbf{e}_\lambda, \mathbf{e}_\beta, \mathbf{e}_\varphi)$ can be derived from the tensor transformation equation

$$\hat{h}_{ijkl} = Q_{im}Q_{jn}Q_{kp}Q_{lq}\hat{h}_{mnpq} \quad (4.13)$$

where \hat{h}_{mnpq} are the components of $\hat{\mathbf{h}}$ in the frame of material orthotropy and \mathbf{Q} is the orthogonal transformation tensor. As explained in chapter II, $\hat{\mathbf{h}}$ can be represented as a diagonal positive definite matrix in Voigt form, in the frame of orthotropy. Let $[\hat{\mathbf{h}}]$ denote the (6×6) matrix representation of $\hat{\mathbf{h}}$ in the $(\mathbf{e}_\lambda, \mathbf{e}_\beta, \mathbf{e}_\varphi)$ frame. We can now write the expression for the Hill equivalent strain rate, d_{eq} , as

$$d_{eq} = \sqrt{\frac{2}{3}[A]^T[\mathcal{L}]^T[\hat{\mathbf{h}}][\mathcal{L}][A]} = \sqrt{[A]^T[\mathcal{M}][A]} \quad (4.14)$$

where $[\mathcal{M}] \equiv \frac{2}{3}[\mathcal{L}]^T[\hat{\mathbf{h}}][\mathcal{L}]$ is an $N \times N$ matrix.

The problem is now reduced to determination of the coefficients $[A]$ that minimize the plastic dissipation integral, (4.7). However, not all the components of $[A]$ are

independent since $[A]$ is constrained by the requirement of homogeneous boundary deformation-rate, equations (3.13)₂ and (3.15). Also, we have imposed the additional constraint, given by equation (4.4), which can be written using the Lee-Mear coefficients and associated Legendre functions as

$$2D_{11} + XD_{33} = \frac{3c^2}{a_2^2 - b_2^2} \left[(2 + X)G_2(\lambda_2) - 3 \left(2\frac{a_2}{b_2} + X\frac{b_2}{a_2} \right) F_2(\lambda_2) \right] = 1 \quad (4.15)$$

where the functions $F_2(\lambda)$ and $G_2(\lambda)$ are defined in (3.14). This makes a total of K linear equality constraints on the components of $[A]$. Using these linear equations, we can solve for K of the N unknowns and write

$$[A] = [\mathcal{C}][B] + [A_0] \quad (4.16)$$

where $[B]$ is an $(N - K) \times 1$ vector of the remaining unknowns, $[\mathcal{C}]$ is an $N \times (N - K)$ constraint matrix derived using the equality constraints, and $[A_0]$ is a constant vector. Using (4.16) in (4.14) and (4.14) in (4.7), the expression for $\Pi(\mathbf{D})$ becomes

$$\inf_{[B] \in \mathbb{R}^{(N-K)}} \frac{\sigma_1}{\Omega} \int_{\lambda_1}^{\lambda_2} \int_0^\pi \int_0^{2\pi} \sqrt{([B]^T[\mathcal{C}]^T + [A_0]^T)[\mathcal{M}]([C][B] + [A_0])} L_\lambda L_\beta L_\varphi d\varphi d\beta d\lambda \quad (4.17)$$

The above represents an unconstrained optimization problem where $\Pi(\mathbf{D})$ is the objective function in $(N - K)$ variables, $[B]$, and the space of admissible values of $[B]$ is $\mathbb{R}^{(N-K)}$. Note that the existence and uniqueness of the minimum is guaranteed by the fact that the matrix $[\mathcal{M}]$ is positive definite, and hence the objective function is convex. The gradient of the objective function with respect to the unknowns, $[B]$ is given by

$$\frac{\partial \Pi}{\partial [B]} = \frac{\sigma_1}{\Omega} \int_{\lambda_1}^{\lambda_2} \int_0^\pi \int_0^{2\pi} \frac{[\mathcal{C}]^T[\mathcal{M}]([C][B] + [A_0])}{\sqrt{([B]^T[\mathcal{C}]^T + [A_0]^T)[\mathcal{M}]([C][B] + [A_0])}} L_\lambda L_\beta L_\varphi d\varphi d\beta d\lambda \quad (4.18)$$

The above problem can be solved for various values of the macroscopic stress

triaxiality, T , to obtain individual points on the yield locus using equation (4.3). A program is developed to solve the above optimization problem using the Conjugate-Gradient minimization routines from the NAG numerical library [37]. From here onwards, the yield locus obtained using the above method will be referred to as the exact numerical yield locus. The analytical criterion of chapter III is compared with the exact numerical yield loci for various microstructural parameters and material anisotropy coefficients in the following section.

B. Comparison of the Analytical and Numerical Yield Loci

For the purpose of generation of the numerical yield loci, we need to choose a set of anisotropy parameters representative of actual material properties. For simplicity, we assume that the void axis coincides with one of the material orthotropy directions, so that the frame $(\mathbf{e}_1, \mathbf{e}_2, \mathbf{e}_3)$ of figure 3 may be taken to be the frame of orthotropy. The anisotropy tensors \mathbf{h} and $\hat{\mathbf{h}}$ have six non-zero components in the frame of orthotropy, and may be represented as a diagonal 6×6 matrix in Voigt notation. Let \hat{h}_i ($i = 1..6$) represent the diagonal elements of the matrix representation of $\hat{\mathbf{h}}$. The anisotropy factors, h, h_t and h_a that appear in the analytical criterion are then given by

$$h = \frac{\hat{h}_1 + \hat{h}_2 + 4\hat{h}_3}{6}, \quad h_t = \frac{\hat{h}_1 + \hat{h}_2 + 2\hat{h}_6}{4}, \quad h_a = \frac{\hat{h}_4 + \hat{h}_5}{2} \quad (4.19)$$

Only five of the six factors, \hat{h}_i , are independent as their values are normalized such that the quadratic form for the Hill equivalent stress, equation (2.5), equals the yield stress in any one of the three orthotropy directions. In our case, for ease of comparison of the results for different materials, we choose this to be the axial direction of the void, i.e. \mathbf{e}_3 . The values of the parameters, \hat{h}_i , can be derived from the five intrinsic strain ratios of the material, as shown in [1, 22]. The relation between the material strain

ratios and the parameters, \hat{h}_i , are given in Appendix A. Table A in Appendix A lists material anisotropy data, in the form of strain ratios in the orthotropy directions, for a range of engineering materials. The data in Table A has been reproduced from [1]. The values of the factors h, h_t and h_a are also tabulated. Notice that the value of h for all materials is very close to unity. This is because we have chosen to normalize the anisotropy factors in such a way that the Hill equivalent stress equals the yield stress in the 3-direction, so that the diagonal elements of the tensor \mathbf{h} obeys $(h_1 + h_2 + 4h_3)/6 = 1$. It can be shown using the relations (A.1) that the above is close to $1/h$, as is indeed observed from the data in Table A. Also notice that the largest value of h_t was obtained for some alloy of Al and the smallest value for Zircaloy, for the chosen void orientation. The value of h_a , which depends on the out of plane strain ratios, is not available for thin sheet metals.

The numerical results presented in this section are generated for four sets of materials parameters, tabulated in Table 1. The first row corresponds to an isotropic matrix ($h = h_t = h_a = 1$). Second and third rows correspond to some transversely isotropic materials with $\mathbf{e}_1 - \mathbf{e}_2$ as the plane of isotropy. These are designated material 1 and material 2 respectively, with the strain ratios, $R = 1/2$ and $Rh = 5$ for material 1 and $R = 3$ and $Rh = 1/4$ for material 2 (see Appendix A for definitions of R and Rh). These are representative of thin sheets of Al and Zircaloy respectively [22]. The last row (material 3) is representative of commercially pure Ti, with the in-plane strain ratios taken from Table A [38]. The out of plane ratios (R^{TS} and R^{SL}) were not available from the literature and were assumed to be unity.

Figure 11 shows the comparison of the analytical and numerical yield loci for prolate cavities and the four different material properties from Table 1. Results are presented for three different values of the porosity, $f = 0.001, f = 0.01$ and $f = 0.1$ and a void aspect ratio $w_1 = 5$. The solid lines correspond to the analytical

Table 1. Table of material anisotropy parameters used in the numerical computations.

Name	\hat{h}_1	\hat{h}_2	\hat{h}_3	\hat{h}_4	\hat{h}_5	\hat{h}_6	h	h_t	h_a
Isotropic	1.00	1.00	1.00	1.00	1.00	1.00	1.00	1.00	1.00
Material 1									
(Al)	1.50	1.50	0.75	0.36	0.36	1.50	1.00	1.50	0.36
Material 2									
(Zircaloy)	0.43	0.43	1.29	1.00	1.00	0.43	1.00	0.43	1.00
Material 3									
(C.P. grade Ti)	0.49	1.25	1.15	0.73	1.06	0.61	1.05	0.74	0.89

yield loci of equation (3.39) and the dotted lines to the loci from Monchiet et al. [3]. The numerical yield points are generated using the method explained in the previous section, using 21 Lee-Mear velocity fields corresponding to the coefficients B_{00} and B_{km} with ($k = 2, 4$) and ($m = 0..4$), equation (3.8). Notice that in all cases, the proposed analytical criterion is in excellent agreement with the numerical data, where as the criterion of [3] shows significant discrepancies, especially towards smaller values of porosity.

Figure 12 shows the comparison of the yield loci for the four materials from Table 1, for the case of $f = 0.001$ and $w_1 = 5$. The new criterion gives good agreement with the numerical yield points in all cases.

Figure 13 shows the comparison of the analytical and numerical yield loci for oblate cavities with $w_1 = 1/5$ and three values of porosity. The solid lines correspond to the analytical loci of equation (3.39) while the dotted line corresponds to the criterion of [3]. The numerical points are generated using 21 velocity fields corresponding to the coefficients B_{00} and B_{km} with ($k = 2, 4$) and ($m = 0..4$), equation (3.9). Again, the new criterion is seen to be in closer, albeit approximate, agreement

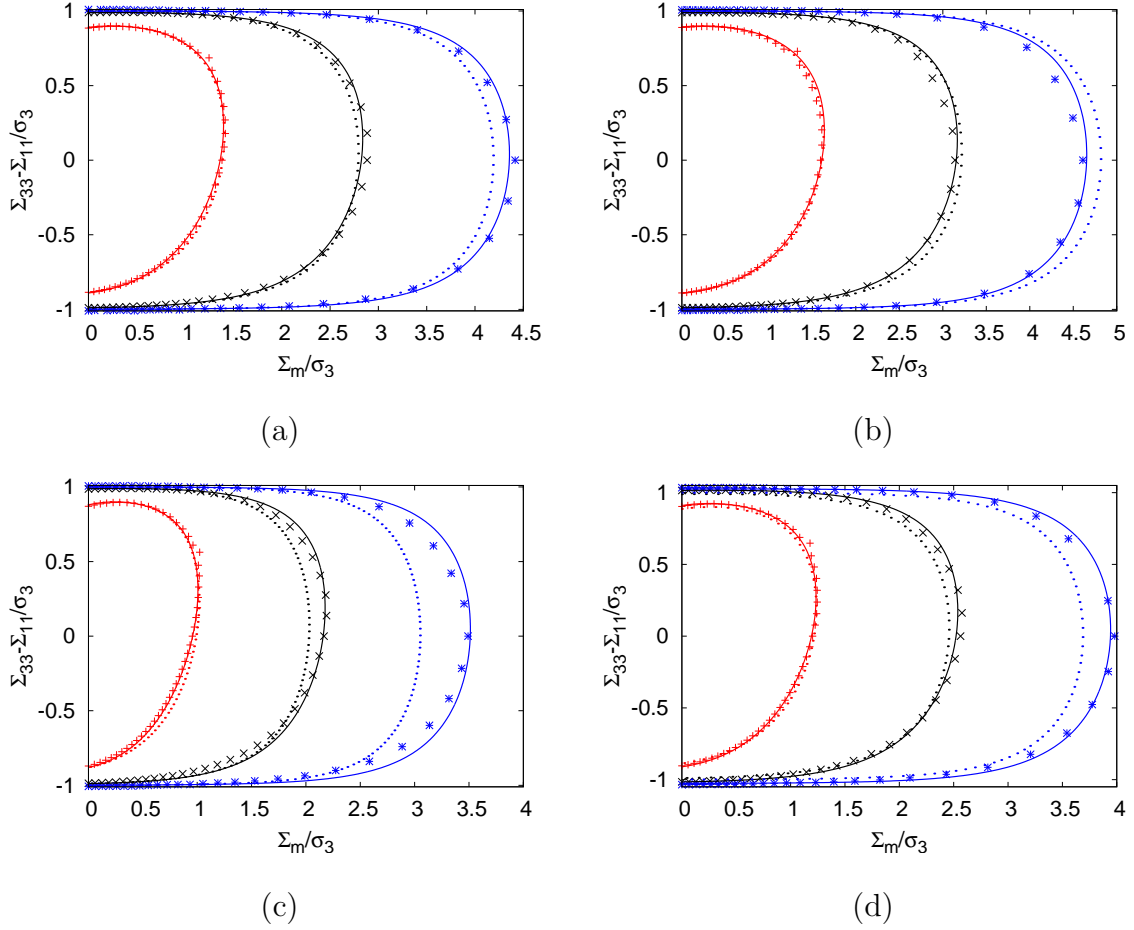


Fig. 11. Comparison of the analytical and numerical yield loci for prolate cavities. (a) Isotropic matrix (b) Material 1 (c) Material 2 (d) Material 3 and porosity, $f = 0.001$ (*), $f = 0.01$ (\times), $f = 0.1$ (+). In all cases, $w_1 = 5$. The solid lines correspond to the analytical criterion of this thesis and the dotted line is from [3].

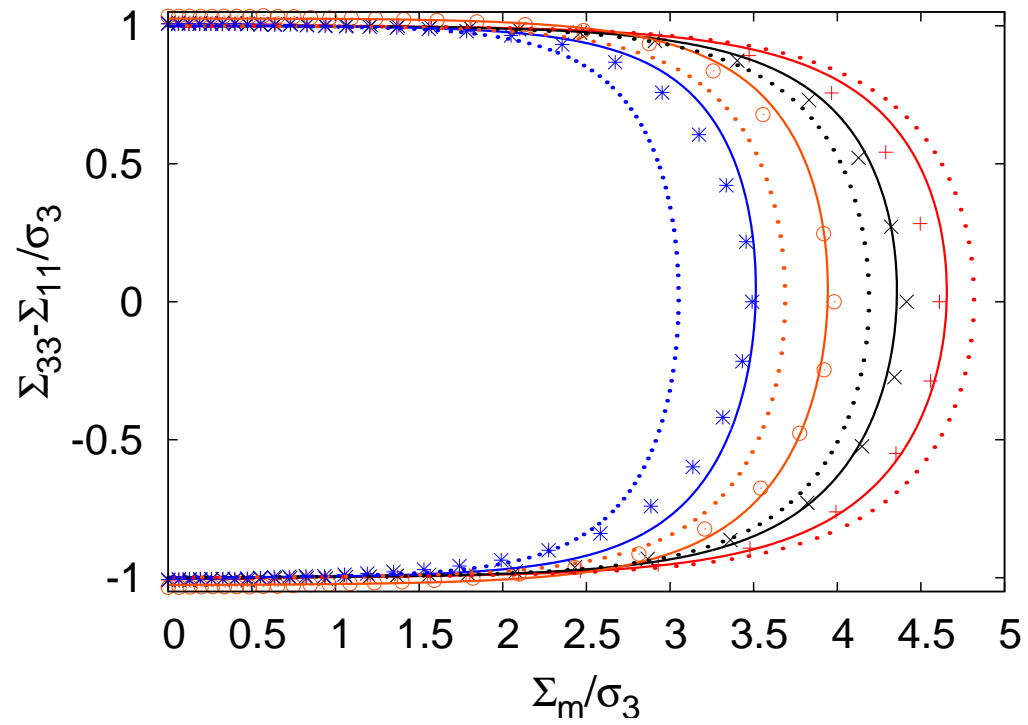


Fig. 12. Comparison of the analytical and numerical yield loci for Isotropic matrix (\times), Material 1 ($+$), Material 2 ($*$) and Material 3 (\circ), for the case $f = 0.001$ and $w_1 = 5$. The solid lines correspond to the analytical criterion of this thesis and the dotted line is from [3].

with the numerical data than the criterion of Monchiet et al. [3].

Figure 14 shows the comparison of the yield loci for the four different materials from Table 1 for the case $f = 0.001$ and $w_1 = 1/5$. Notice that in all cases the criterion of [3] provides a strict upper bound, but lies relatively far from the numerical curve. The new criterion appears to violate the strict upperbound character for some values of the triaxiality, but lies close to the numerical points in all cases.

In order to further assess the validity of the new yield criterion, we now present a set of parameter studies illustrating the distinct influences of material anisotropy and void shape on the macroscopic yield point. As seen from the results presented in figures 11-14, variation of either results in a significant change in the yield point towards higher stress triaxialities. In the results to be presented in the following figures, we study the variation of the yield point under a state of macroscopic hydrostatic stress, designated Σ_m^y , as a function of the void aspect ratio for a given set of material anisotropy factors (h, h_t, h_a) , and vice versa. Thus, these results serve to illustrate the individual effects of void shape and the anisotropy of the matrix on macro yield.

Figure 15 illustrates effect of the void aspect ratio, w_1 , on the hydrostatic yield point, Σ_m^y , for the four materials from Table 1. As before, the solid line corresponds to the new yield criterion, the dotted line to the criterion of Monchiet et al. [3] and the discrete points to the numerically determined upper bound values. As is clearly seen from the figure, the new criterion gives a significantly better prediction for the hydrostatic yield point over a wide range of void aspect ratios.

In order to characterize the influence of material anisotropy, we present the variation of Σ_m^y as a function of the parameters h_t and h_a respectively, in figures 16 and 17. As per their definitions in equation (3.33), h_t depends only on the anisotropy coefficients in the plane normal to the void axis, while h_a depends only on the out-of-

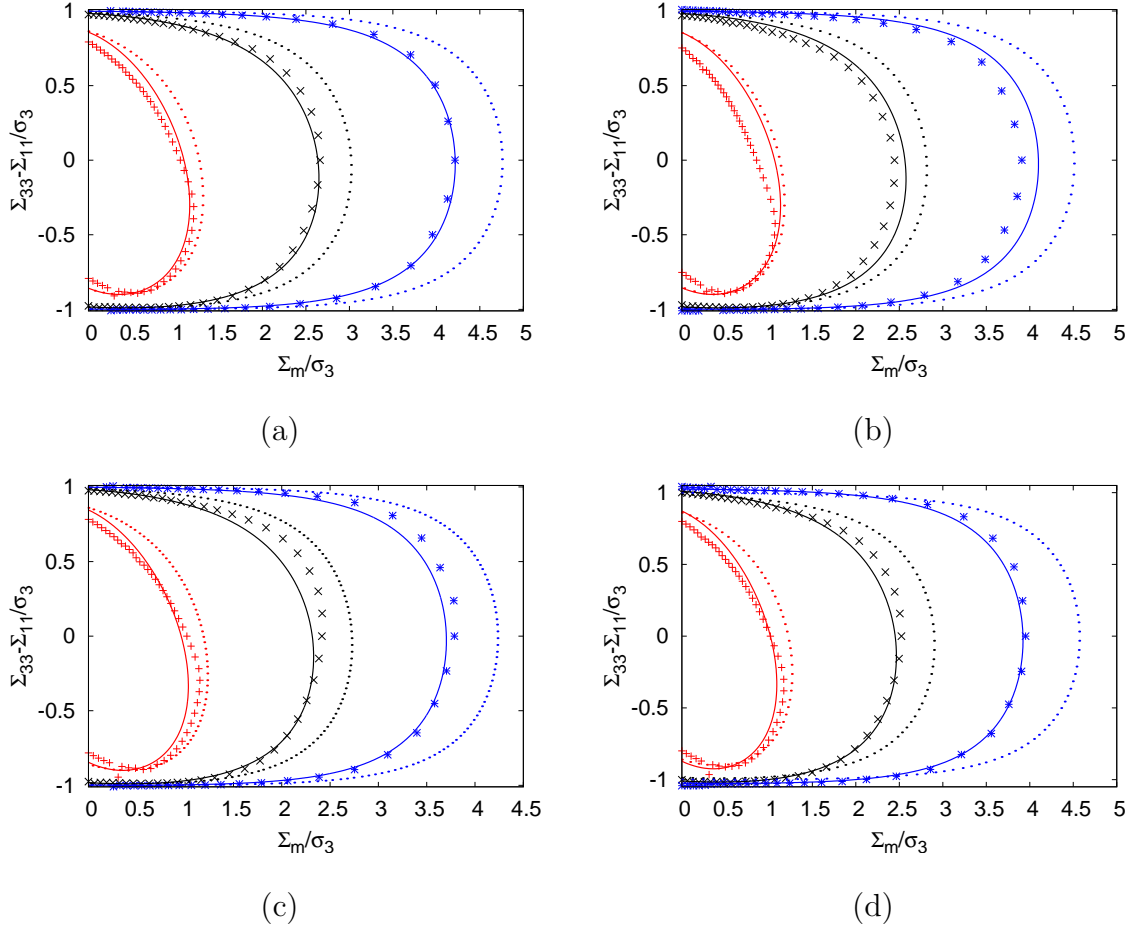


Fig. 13. Comparison of the analytical and numerical yield loci for oblate cavities. (a) Isotropic matrix (b) Material 1 (c) Material 2 (d) Material 3 and porosity, $f = 0.001$ (*), $f = 0.01$ (x), $f = 0.1$ (+). In all cases, $w_1 = 1/5$. The solid lines correspond to the analytical criterion of this thesis and the dotted line is from [3].

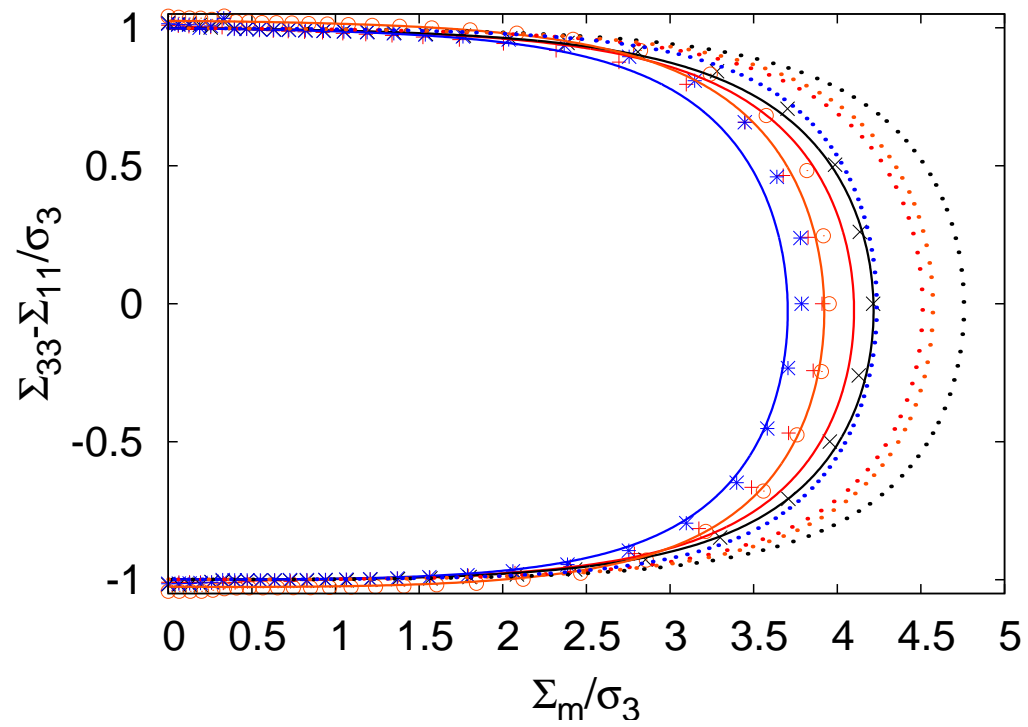


Fig. 14. Comparison of the analytical and numerical yield loci for Isotropic matrix (\times), Material 1 ($+$), Material 2 ($*$) and Material 3 (\circ), and $f = 0.001$, for the case $f = 0.001$ and $w_1 = 1/5$. The solid lines correspond to the analytical criterion of this thesis and the dotted line is from [3].

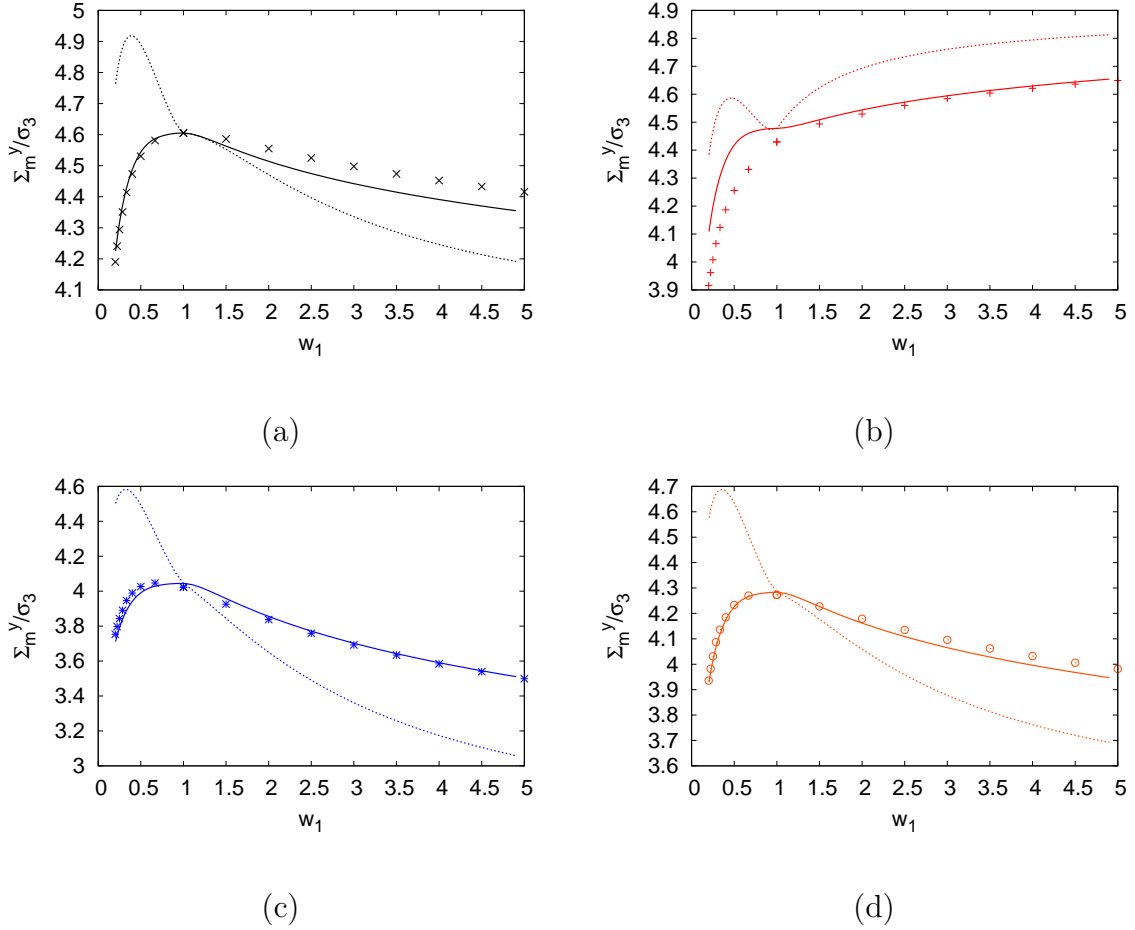
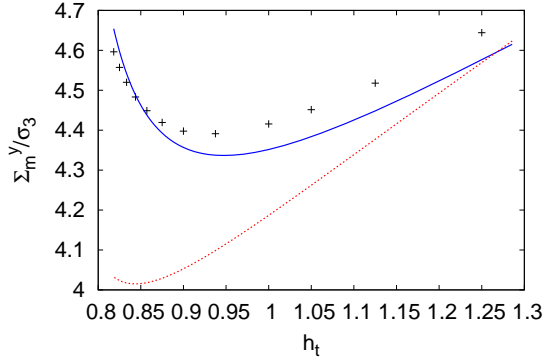
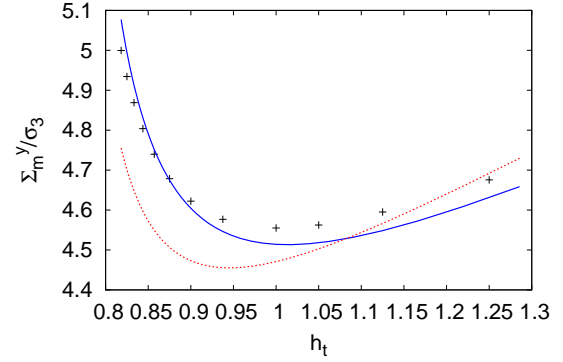


Fig. 15. Variation of the yield point under hydrostatic loading, Σ_m^y , as a function of the void aspect ratio, w_1 , for porosity $f = 0.001$, and (a) Isotropic matrix (b) Material 1 (c) Material 2 (d) Material 3. The discrete points are the numerically determined yield points, the solid line correspond to the analytical criterion of this thesis and the dotted line is from [3].

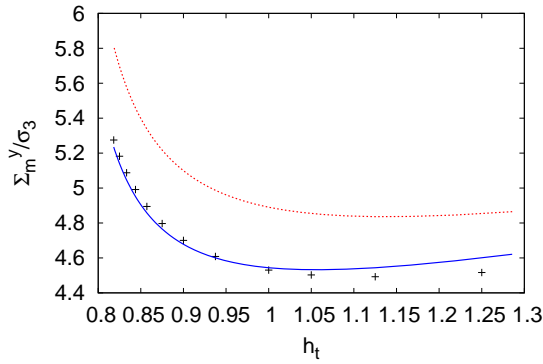
plane “shear” coefficients. Hence, these two parameters can be varied independently to study their respective influence on the yield criterion. It must be mentioned here that the parameters h_t and h_a are in fact linear combinations of Hill orthotropy coefficients that can vary independently and hence these do not uniquely characterize a specific state of orthotropy. However, as the yield criterion is seen to depend explicitly on these specific combinations of the anisotropy coefficients, it appears reasonable to study the effect of plastic anisotropy through the variation of these factors. For convenience, the results presented here are generated assuming transversely isotropic material behavior for which the state of anisotropy can in fact be described using two parameters [22]. The results are presented for four different values of the void aspect ratio, ($w_1 = 1/5, 1/2, 2, 5$). Figure 16 shows the variation of Σ_m^y as a function of h_t for $h_a = 1$ and four different void aspect ratios. Figure 17 shows the variation of Σ_m^y as a function of h_a for $h_t = 1$ and the four different void shapes. The solid line shows the predictions from the new yield criterion, the dotted line is from [3], and the discrete points are the numerically determined values. In all cases, the new criterion gives better predictions for the yield point over a wide range of values of the anisotropy factors.



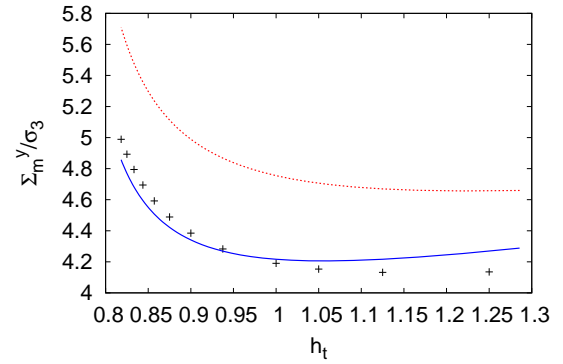
(a)



(b)

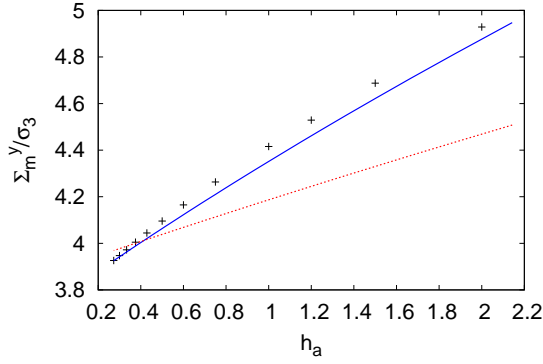


(c)

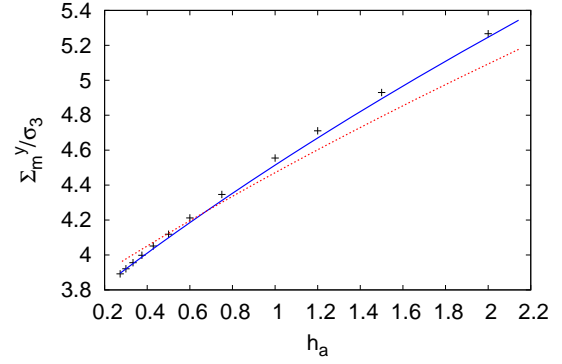


(d)

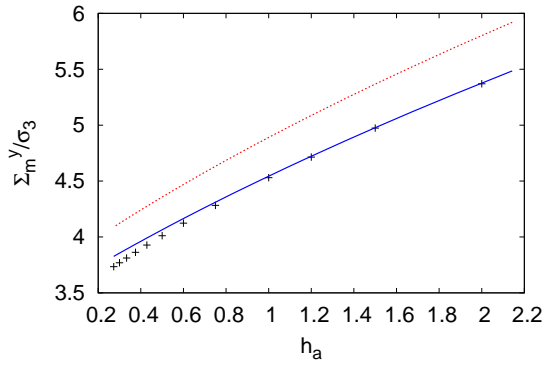
Fig. 16. Variation of the yield point under hydrostatic loading, Σ_m^y , as a function of the parameter h_t , for $h_a = 1$, $f = 0.001$ and (a) $w_1 = 5$ (b) $w_1 = 2$ (c) $w_1 = 0.5$ (d) $w_1 = 0.2$. The discrete points are the numerically determined yield points, the solid line correspond to the analytical criterion of this thesis and the dotted line is from [3].



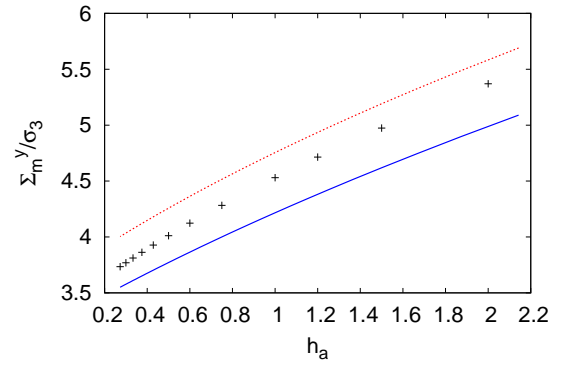
(a)



(b)



(c)



(d)

Fig. 17. Variation of the yield point under hydrostatic loading, Σ_m^y , as a function of the parameter h_a , for $h_t = 1$, $f = 0.001$ and (a) $w_1 = 5$ (b) $w_1 = 2$ (c) $w_1 = 0.5$ (d) $w_1 = 0.2$. The discrete points are the numerically determined yield points, the solid line correspond to the analytical criterion of this thesis and the dotted line is from [3].

CHAPTER V

EVOLUTION LAWS FOR POROSITY AND VOID SHAPE PARAMETER

Complete specification of the constitutive laws requires specification of the flow rule and the evolution laws of the internal variables (f and S in this case), in addition to the yield criterion. Once these are specified, the constitutive laws can be integrated for various loading paths, using a suitable integration scheme, to obtain the stress-strain response of the material. These are also required for implementing the model in finite element packages, for simulation of practical engineering problems. The closed form expressions for the flow rule and the evolution laws for f and S will be specified in this chapter.

Hill [30], and later Gurson [14] for the case of porous materials, has demonstrated that the normality (or associated) flow rule holds at the macroscale, provided that the boundary of the elastic convex is regular. The normality flow rule writes

$$\mathbf{D}^p = \Lambda \frac{\partial \mathcal{F}}{\partial \boldsymbol{\Sigma}} \quad (5.1)$$

where $\mathcal{F}(\boldsymbol{\Sigma})$ denotes the macroscopic yield function (left hand side of equation (3.39)), Λ is the plastic multiplier and \mathbf{D}^p denotes the plastic deformation rate. Equation (5.1) can be integrated in the usual way, by solving for the parameter Λ using the consistency conditions.

A. Evolution of Porosity

The evolution law for porosity can be derived from (5.1) in a straightforward manner using the plastic incompressibility of the Hill matrix. Using the definition of porosity,

we have

$$\dot{f} = \left(\frac{\dot{\omega}}{\Omega} \right) = (1 - f) \frac{\dot{\omega}}{\Omega} \quad (5.2)$$

where we have used the condition that $\dot{\Omega} = \dot{\omega}$, assuming the matrix to be plastically incompressible, and neglecting the volumetric strain due to elasticity. Using the small deformation approximation, we have

$$\frac{\dot{\Omega}}{\Omega} = \frac{\dot{\omega}}{\Omega} = D_{ii}^p = 3D_m^p \quad (5.3)$$

One can show using equation (5.1) that the following equality holds

$$D_m^p = \frac{1}{3} \Lambda \frac{\partial \mathcal{F}}{\partial \Sigma_m} \quad (5.4)$$

Combining equations (5.2), (5.3) and (5.4) we obtain

$$\dot{f} = (1 - f) \Lambda \frac{\partial \mathcal{F}}{\partial \Sigma_m} \quad (5.5)$$

The above equation specifies the evolution rate for the porosity.

In order to see the effect of void shape and matrix anisotropy on the porosity rate, figure 18 illustrate the variation of D_m/D_m^{sph} as a function of the void aspect ratio for $f = 0.01$, macroscopic stress triaxiality, $T = 1$, and three different material anisotropy parameters. D_m^{sph} here corresponds to the value of D_m for a spherical void ($w_1 = 1$). Note that since, in general, the spherical and the non-spherical RVEs have different yield points, and the materials being considered are not hardenable, the comparison is made for the case that the two RVEs have the same axial strain rate, i.e. $D_{33} = D_{33}^{sph}$. The actual value of D_m^{sph} , used in the calculations reported here, is obtained using a void with a vanishingly small eccentricity, which may be considered for all practical purposes to be a sphere. Discrete points in the figure correspond to numerically obtained values of D_m/D_m^{sph} using the method described in chapter IV.

The solid lines correspond to the model predictions using equations (5.5) and (3.39). The dotted line represents the model results from Monchiet et al. [3].

In the prolate case, it may be observed that the present model yields closer agreement the numerical results for all three materials tested. In the oblate case, however, both models yield acceptable, albeit approximate, results for the variation of D_m/D_m^{sph} with the void aspect ratio.

B. Evolution of the Shape Parameter

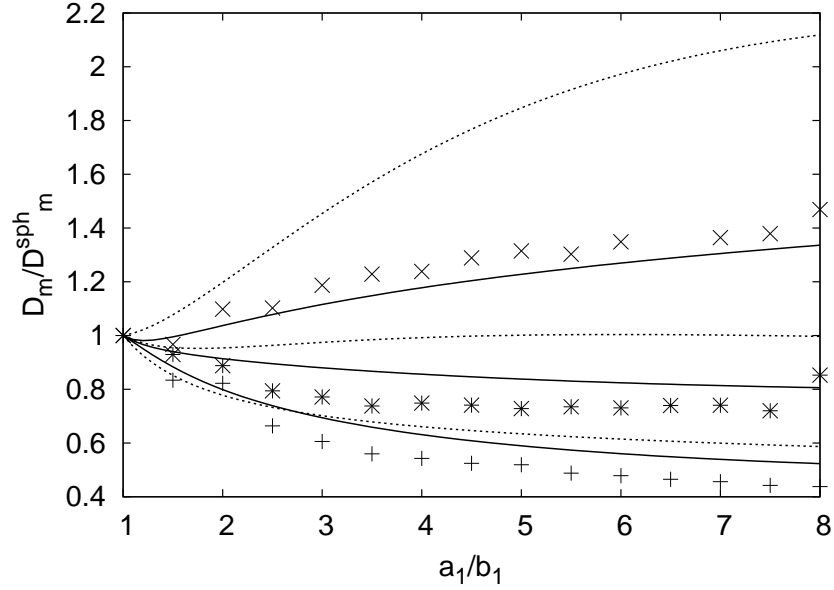
Unlike the case of the yield criterion, which was derived based on sound variational principles, and the evolution rate for porosity which followed from the yield criterion using the normality flow rule and plastic incompressibility of the matrix, the evolution of the shape parameter, S , can not be determined based on fundamental principles. Therefore, an empirical approach is followed to define a closed form expression for \dot{S} , as was done in [25]. The resulting expression for \dot{S} contains empirical factors that are determined based on comparisons to numerical simulation results, as explained below. The shape parameter, S , is defined by $S = \ln a_1/b_1$ and hence we have

$$\dot{S} = \frac{\dot{a}_1}{a_1} - \frac{\dot{b}_1}{b_1} \quad (5.6)$$

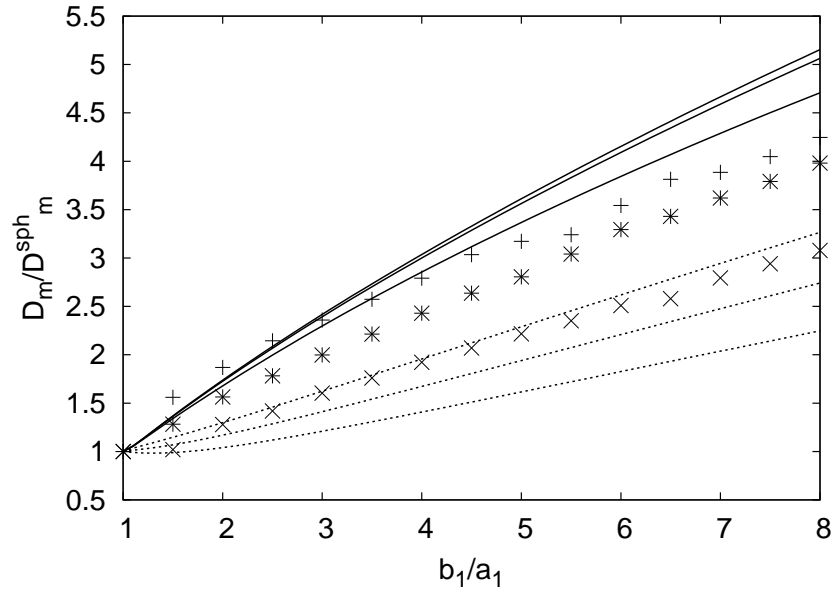
However, if we assume that the RVE is being deformed homogeneously, \dot{S} would also be given by

$$\dot{S} = D_{33}^v - D_{11}^v \quad (5.7)$$

In reality, the RVE is not deformed homogeneously and the void loses its initial spheroidal shape. In this case, the above two expressions are different and the latter expression is adopted to represent the void shape change, which in some sense mea-



(a)



(b)

Fig. 18. D_m/D_m^{sph} as a function of the void aspect ratio, (a) a_1/b_1 for prolate cavities (b) b_1/a_1 for oblate cavities, stress triaxiality, $T = 1$ and $f = 0.01$. The solid line corresponds to the predictions from the present model, and the dotted line corresponds to the model in [3]. Discrete points correspond to numerically determined values for an isotropic matrix (*), material 1 (+) and material 2 (\times) from Table 1.

sures the “average shape change” of the void. This can be rewritten as

$$\dot{S} = A(D_{33}^{vA} - D_{11}^{vA}) + B(D_{33}^{vB} - D_{11}^{vB}) \quad (5.8)$$

Using equation (3.48) and the incompressibility of the matrix leads to

$$\dot{S} = 3(1 - 3\alpha_1)AD_m^{vA} + \frac{3}{2}B = 3\frac{1 - 3\alpha_1}{f}AD_m^A + \frac{3}{2}B \quad (5.9)$$

We have, using (3.22) and (3.24)

$$A = \frac{D_m}{D_m^A}, \quad B = -2(1 - 2\alpha_2)D_{11} + 2\alpha_2D_{33} \quad (5.10)$$

Combining (5.9) and (5.10), we get

$$\dot{S} = D_{33} - D_{11} + 3\left(\frac{1 - 3\alpha_1}{f} + 3\alpha_2 - 1\right)D_m \quad (5.11)$$

It can be demonstrated that in some special cases like cylindrical voids, “sandwich” shaped voids and penny shaped cracks, the above expression reduces to the exact values for \dot{S} [25].

In the case of the isotropic matrix, the above expression was modified by Golganu et al. [25] to incorporate a heuristic factor multiplying the $D_{33} - D_{11}$ term, which depended in the void shape, the stress triaxiality and the porosity, as follows

$$\dot{S} = s(D_{33} - D_{11}) + 3\left(\frac{1 - 3\alpha_1}{f} + 3\alpha_2 - 1\right)D_m \quad (5.12)$$

where,

$$s \equiv 1 + s_e s_f s_T$$

$$s_e(e_1) \equiv \frac{9}{2} \frac{\alpha_1 - \alpha_1^{Gar}}{1 - 3\alpha_1}, \quad s_f(f) \equiv (1 - \sqrt{f})^2, \quad s_T(T) \equiv \begin{cases} 1 - (T^2 + T^4)/9 & \text{for } \epsilon = +1 \\ 1 - (T^2 + T^4)/18 & \text{for } \epsilon = -1 \end{cases} \quad (5.13)$$

The parameters ϵ and α_1^{Gar} , above, are defined by

$$\epsilon \equiv \text{sgn}(\Sigma_m \Sigma'_{33}), \quad \alpha_1^{Gar} = \begin{cases} 1/(3 - e_1^2) & \text{(p)} \\ (1 - e_1^2)/(3 - 2e_1^2) & \text{(o)} \end{cases} \quad (5.14)$$

The expressions for the heuristic parameters s_e , s_f and s_T were determined by comparison to numerical calculations of the type described in chapter IV. The details of the same may be found in [25].

The considerations used in determining the above parameters may be expected to hold when the Von Mises matrix considered by these authors is replaced by a Hill orthotropic matrix. In addition, it is expected that the anisotropy factors, h , h_t and h_a will impact the void shape evolution. Recall that the numerical simulations results for the parameter α_2 that appears in the D_m term of equation (5.12), presented in figure 7 of chapter III, showed a (small) influence of the anisotropy parameters, especially towards small void eccentricities. This implies that, even for a spherical void under hydrostatic loading, the void shape can evolve due to the anisotropy of the matrix. However, we have chosen to ignore this influence in determining the functions α_1 and α_2 , equations (3.51) and (3.42). In practice, states of pure hydrostatic loading are rare and the triaxiality is usually of the order of unity or lower. In such circumstances, the term proportional to $D_{33} - D_{11}$ is expected to play a dominant role in determining \dot{S} . Therefore, we propose to augment the heuristic factor, s , in equation (5.12), to include a term that represents the influence of the anisotropy factors as shown below.

$$s \equiv 1 + s_h s_e s_f s_T \quad (5.15)$$

where s_e , s_f and s_T are as given by equation (5.13) and s_h is a new factor that depends on the anisotropy parameters.

Clearly, s_h should be unity for an isotropic matrix, in which case equation (5.15)

reduces to that of Gologanu et al. (5.13). In the anisotropic case, one can determine the exact value of \dot{S} using the numerical method outlined in chapter IV, by numerically evaluating the surface integrals in equation (3.49) and then using (5.7) to find \dot{S} . The numerical value of s_h can be calculated from the value of \dot{S} using equations (5.12) and (5.15). We may then seek to find an analytical expression for $s_h = s_h(h, h_t, h_a)$ that fits the numerical data. Considering the definitions of the parameters h, h_t and h_a , equations (3.21) and (3.33), we can see that the values of parameters h and h_t can not be varied independently while that of h_a (which depends on the shear coefficients alone) can be varied independently of the other two. The values of h_t and h_a are therefore varied independently and the corresponding variation of s_h is studied numerically, for the case of $f = 0.01$, $T = 0$ and the void aspect ratio, $w_1 = 2$. It is seen that a simple expression of the form

$$s_h = \frac{h}{4} \left(\frac{3}{h_t} + \frac{1}{h_a} \right) \quad (5.16)$$

fits the numerical results quite well as can be seen from the figures 19 and 20. Figure 19 illustrates the variation of s_h with h_t , keeping h_a constant, and figure 20 illustrates the variation of s_h with h_a , keeping h_t constant. Discrete points are the data obtained numerically and the solid line corresponds to equation (5.16). The numerical data is generated using seven velocity fields from the Lee-Mear decomposition corresponding to $k = 2$ and $m = 0..2$. Notice that equation (5.16) agrees very well with the numerical data.

C. Comparison to Finite Element Simulations on Unit Cells

The best means of validating the expressions obtained for the evolution of porosity and void shape is to compare them to finite element simulations on porous unit cells. For

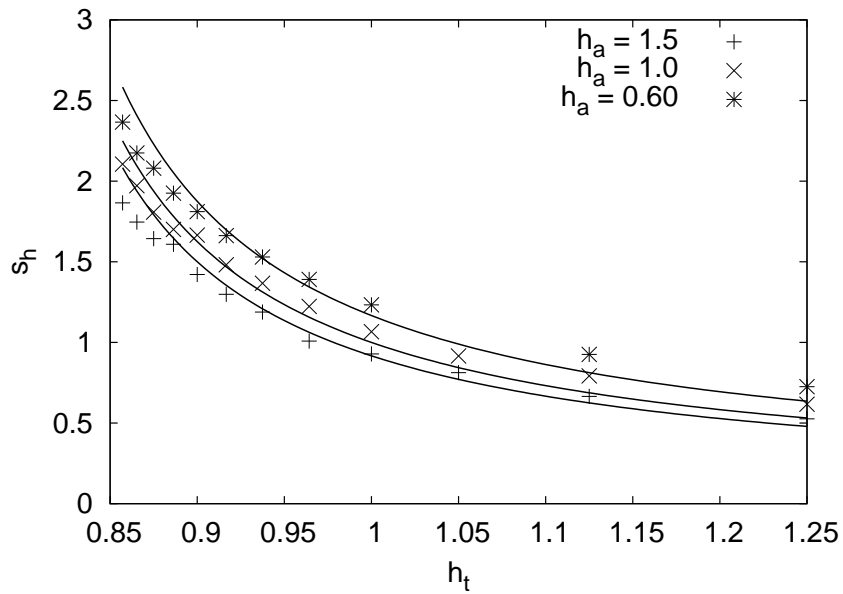


Fig. 19. The factor s_h as a function of h_t . The continuous line corresponds to equation (5.16) and the discrete points correspond to numerically determined values for various values of h_a . In all cases, $f = 0.01$, $T = 0$ and $w_1 = 2$.

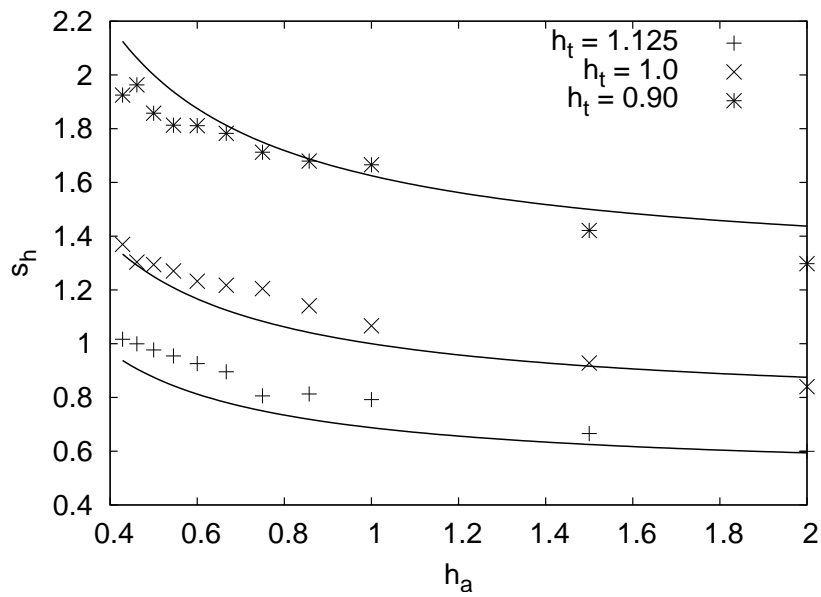


Fig. 20. The factor s_h as a function of h_a . The continuous line corresponds to equation (5.16) and the discrete points correspond to numerically determined values for various values of h_t . In all cases, $f = 0.01$, $T = 0$ and $w_1 = 2$.

this purpose, we use the object-oriented finite element program, Zebulon, developed by Besson and Foerch [39, 40]. A cylindrical RVE is defined containing a single spheroidal void in the center, and triaxial axisymmetric loading paths are considered. The matrix material is assumed to be transversely isotropic in the plane normal to the void axis and is modeled using Hill quadratic yield criterion [34]. Under these conditions, the deformation will be axisymmetric and can be simulated using a 2-D (axisymmetric) analysis. The major stress is applied in the axial direction of the voids and the stress triaxiality is held constant through the simulation. The calculations presented are in fact similar to those in [22], using spheroidal voids instead of spherical voids. Figure 21 show typical RVEs used in the calculations and the details of the mesh used. Exploiting the symmetry of the problem, only a quarter of the domain is modeled. The calculations are terminated prior to the onset of void coalescence, as the emphasis here is on comparing the porosity and void shape evolution rates in the pre-coalescence stage.

For comparison, we also need to integrate the constitutive equations from the model developed here for the case of proportional (axisymmetric) loading paths. For this purpose a program is developed to integrate the constitutive equations (equations (3.39), (5.1), (5.5) and (5.12)) using a class of return-mapping algorithms called the convex cutting plane algorithm developed by Simo and Ortiz [41, 42]. A material element is homogeneously strained at a constant rate in the axial direction, while the applied strain in the lateral direction is varied continuously through each loading step so as to maintain a constant stress triaxiality. The results obtained for \dot{f} and \dot{S} are compared to the direct finite element simulation results in the following figures. Emphasis is placed on comparing the qualitative trends in the evolution of f and S , rather than direct quantitative comparison.

Figure 22(a) and 22(b) show comparison of the evolution of porosity, f , as a

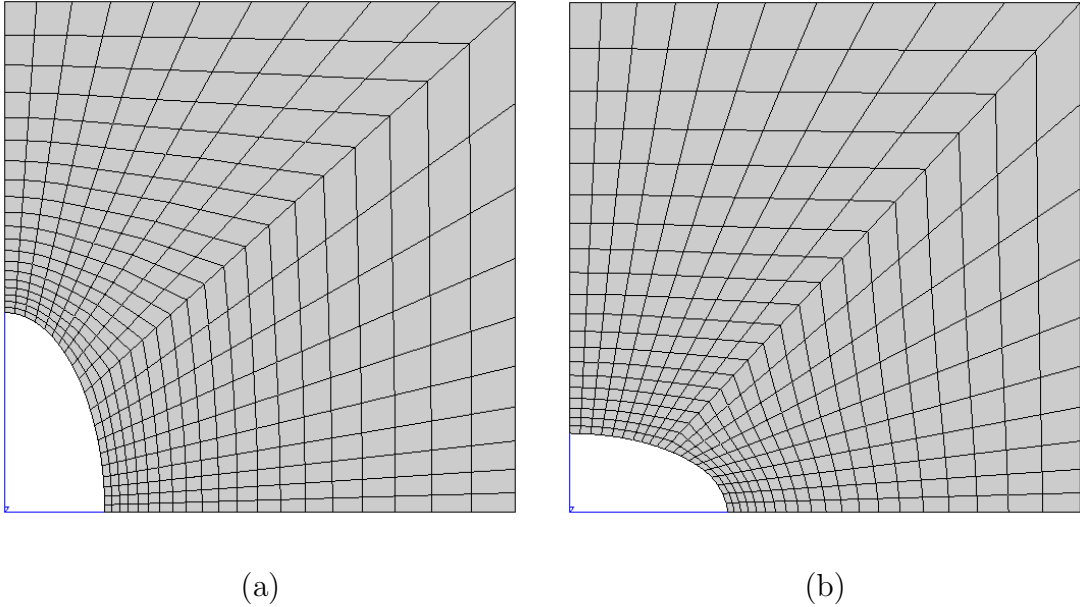
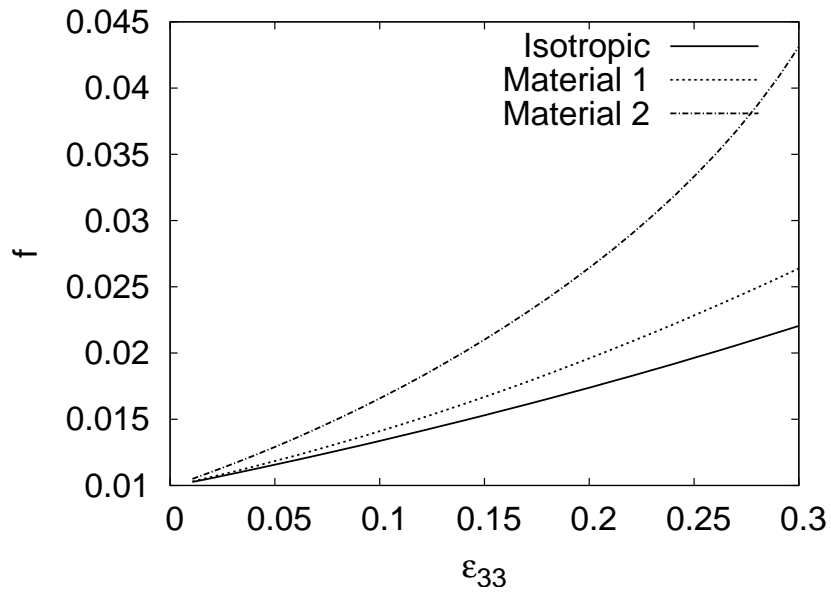


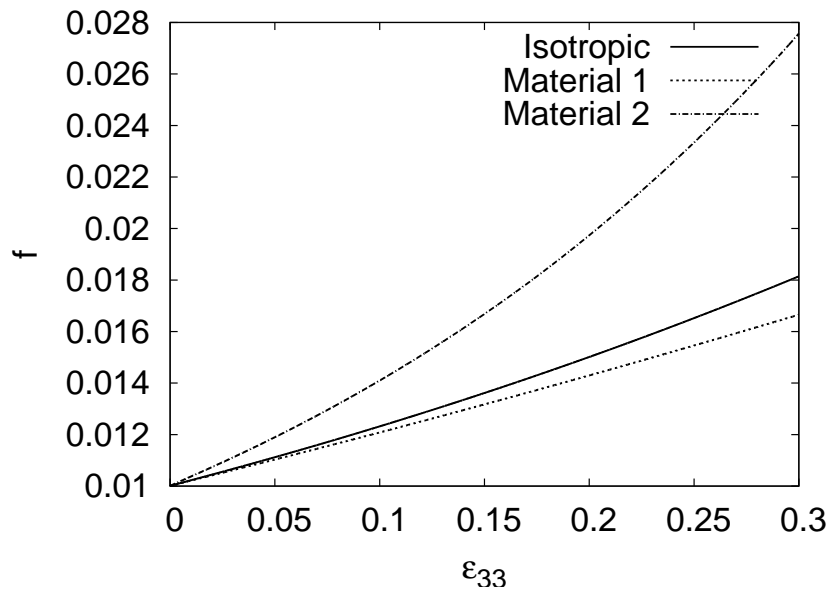
Fig. 21. RVEs used for the unit cell calculations (a) prolate ($a_1/b_1 = 2$) (b) oblate ($a_1/b_1 = 1/2$). Porosity, $f = 0.01$ for both cases.

function of the axial strain, ϵ_{33} , obtained from the FE simulation of the unit cell and integration of the porous constitutive equation respectively. The initial porosity and void aspect ratio were $f = 0.01$ and $w_1 = 2$, corresponding to figure 21(a). The stress triaxiality was held constant at $T = 1$ through the simulation. Figure 23(a) and 23(b) show comparison of the evolution of void aspect ratio, w_1 , as a function of the axial strain for the same RVE. Note that the unit cell results give the evolution of the void aspect ratio as given by equation (5.6) rather than (5.7) assumed in the model. However, qualitatively, the two measures may be expected to show similar trends.

It is observed that the qualitative trends for the evolution of porosity and void shape with deformation for the three materials is correctly predicted by the constitutive equations developed here. However, the unit cell results show a slower growth rate of the porosity as compared to the model results for all the materials considered.

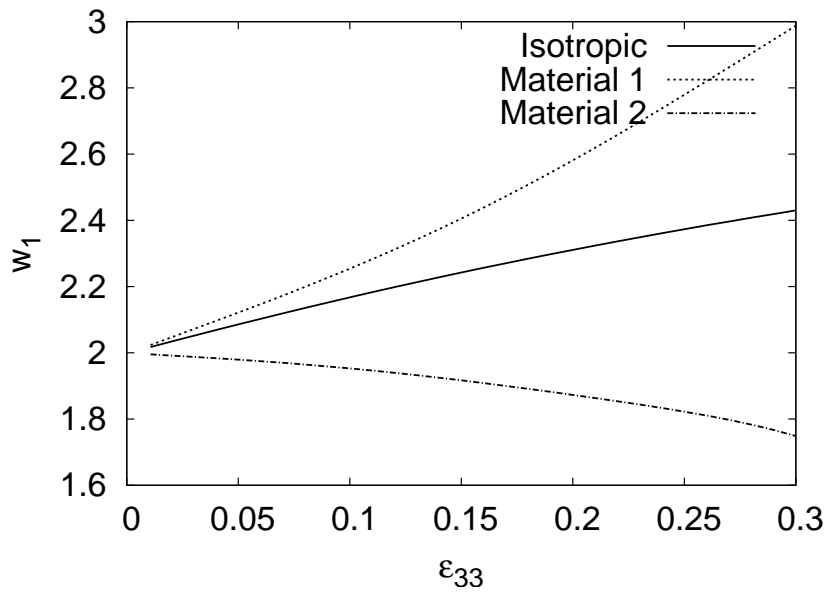


(a)

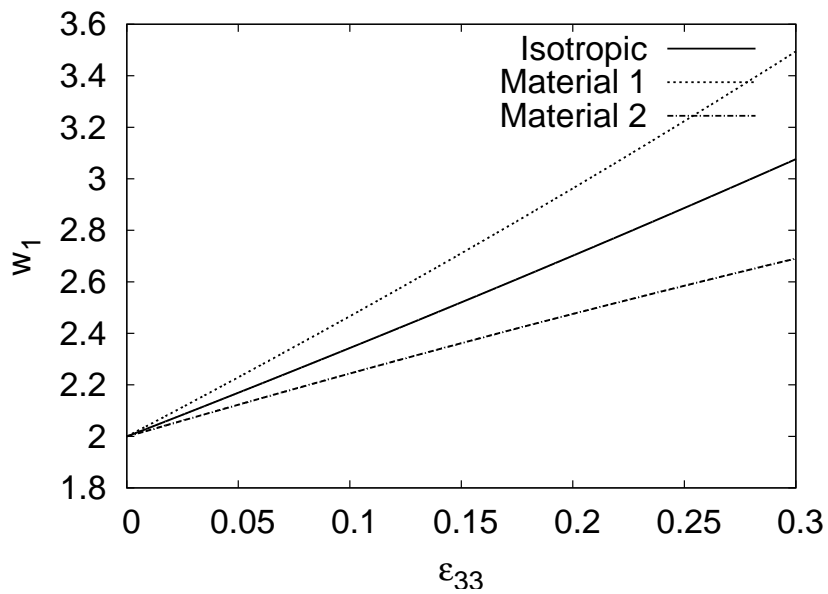


(b)

Fig. 22. Evolution of porosity, f , with axial strain for an initially prolate cavity (a) FE simulation of porous unit cell (b) integration of constitutive equation. The material properties are taken from Table 1. The stress triaxiality was held constant at $T = 1$.



(a)

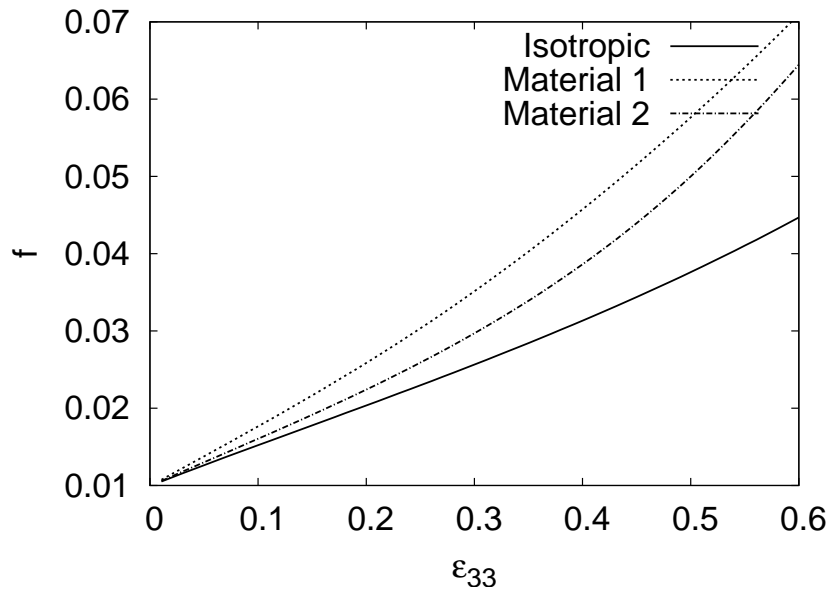


(b)

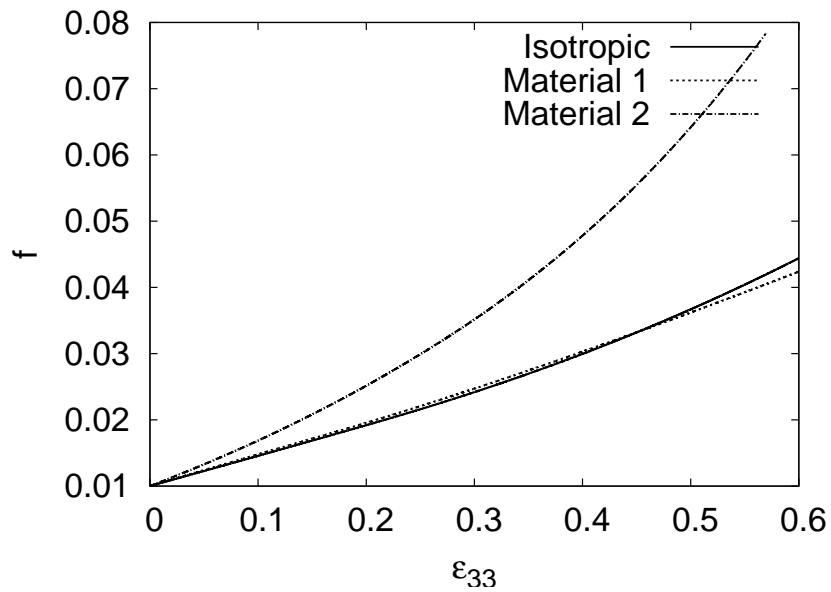
Fig. 23. Evolution of the void aspect ratio, w_1 , with axial strain for an initially prolate cavity (a) FE simulation of porous unit cell (b) integration of constitutive equation. The material properties are taken from Table 1. The stress triaxiality was held constant at $T = 1$.

Also, it is seen that the void aspect ratio for material 2 actually decreases in the finite element simulation results, unlike in the model predictions, for the case of triaxiality, $T = 1$, being considered. Some of these discrepancies could be attributed to the fact that elasticity and hardening were neglected in the development of the analytical model. However, in the finite element computations, elasticity can not be neglected and a power law hardening model (with a small hardening exponent) was assumed for the matrix for stability of the computations. However, despite these discrepancies, the analytical model does capture the effect of plastic anisotropy qualitatively. Some calibration of the model using additional finite element calculations will probably be required to improve the quantitative accuracy of the model predictions for the evolutions of f and w_1 .

Figures 24(a) and 24(b) show a similar comparison of the evolution of porosity, f , as a function of the axial strain, ϵ_{33} , for an initially oblate cavity. The initial porosity and void aspect ratio were $f = 0.01$ and $w_1 = 1/2$, corresponding to figure 21(b). The stress triaxiality was held constant at $T = 1$ through the simulation. Figures 25(a) and 25(b) show comparison of the evolution of void aspect ratio, w_1 , as a function of the axial strain for the same RVE. Again, the model correctly predicts the qualitative trends for the evolution of w_1 with deformation for the three materials studied. However, the prediction for \dot{f} is seen to have a larger discrepancy, especially in the case of material 1. This could be due to the fact that a greater degree of distortion was observed for the numerically determined yield loci for oblate cavities, in chapter IV, especially in the case of larger values of porosity. This curve is only approximately reproduced by the analytical criterion and hence the normals to the two curves may be different. Since \dot{f} is derived as a direct consequence of the normality flow rule, this could impact the quality of the prediction for \dot{f} .

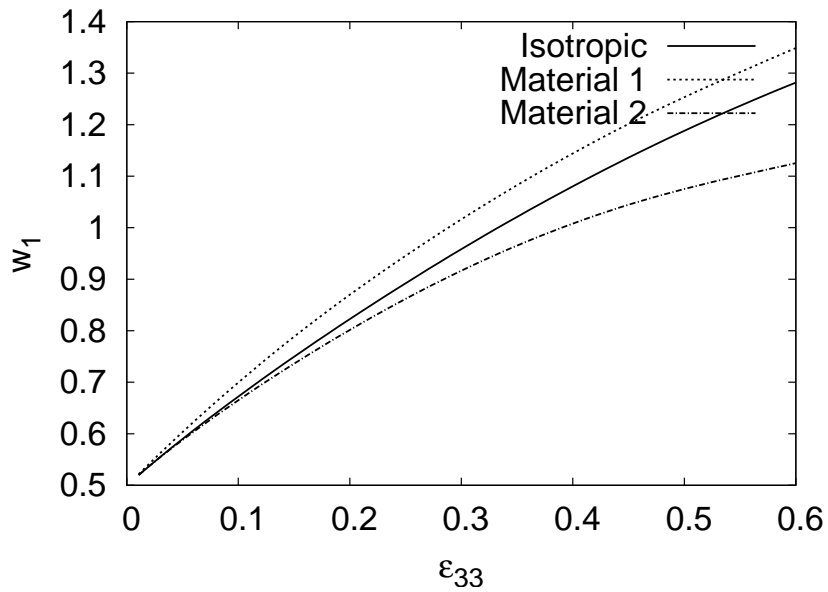


(a)

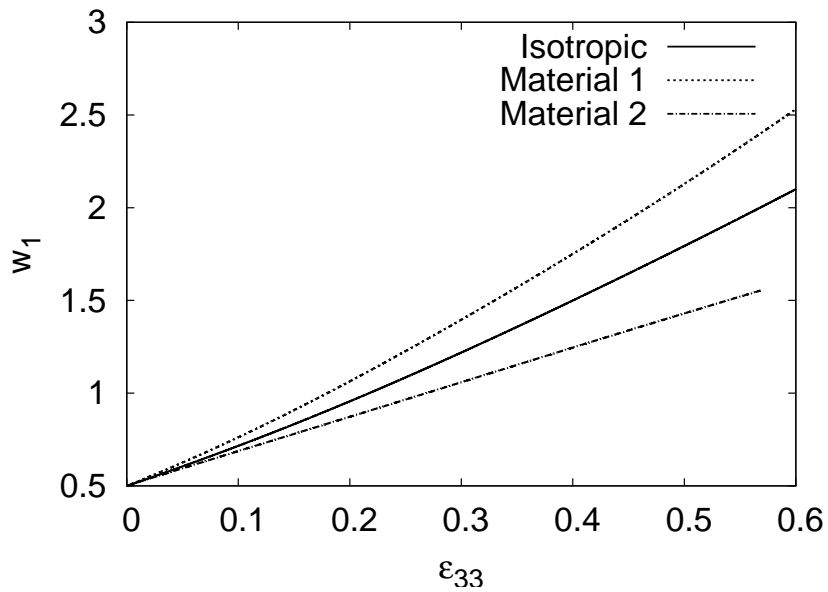


(b)

Fig. 24. Evolution of porosity, f , with axial strain for an initially oblate cavity (a) FE simulation of porous unit cell (b) integration of constitutive equation. The material properties are taken from Table 1. The stress triaxiality was held constant at $T = 1$.



(a)



(b)

Fig. 25. Evolution of the void aspect ratio, w_1 , with axial strain for an initially oblate cavity (a) FE simulation of porous unit cell (b) integration of constitutive equation. The material properties are taken from Table 1. The stress triaxiality was held constant at $T = 1$.

CHAPTER VI

DISCUSSION AND CONCLUSIONS

A. Generalizations

In the previous chapters, a homogenized constitutive relation was developed for plastically anisotropic porous materials containing non-spherical voids. The yield criterion was derived assuming transversely isotropic loading and consequently axisymmetric deformation of the spheroidal RVE. The form of the yield criterion is given by equation (3.39) in chapter III, with the parameters in the criterion defined by equations (3.45), (3.42), (3.50) and (3.51). These parameters are expressible as functions of the microstructural variables, f and S , and the material anisotropy factors, h , h_t and h_a . In this chapter, we propose a heuristic generalization of the yield criterion to arbitrary loading states so that the criterion can be used in practical finite element simulations of ductile fracture. We show that in the case of axisymmetric loadings about the void axis, the generalized criterion reduces approximately to the criterion of equation (3.39).

We propose the following generalized macroscopic criterion for the case of arbitrary loading states.

$$\mathcal{F}(\boldsymbol{\Sigma}) = h \frac{C}{\sigma_1^2} (\boldsymbol{\Sigma}' + \eta \Sigma_h \mathbf{X})_{eq}^2 + 2(g+1)(g+f) \cosh \kappa \frac{\Sigma_h}{\sigma_1} - (g+1)^2 - (g+f)^2 = 0 \quad (6.1)$$

where $\boldsymbol{\Sigma}'$ is the stress deviator and the tensor \mathbf{X} is defined by

$$\mathbf{X} \equiv \frac{1}{3} (-\mathbf{e}_1 \otimes \mathbf{e}_1 - \mathbf{e}_2 \otimes \mathbf{e}_2 + 2\mathbf{e}_3 \otimes \mathbf{e}_3) \quad (6.2)$$

with \mathbf{e}_3 as the void axis. The parameter Σ_h is defined as

$$\Sigma_h \equiv \alpha_2 (\Sigma_{11} + \Sigma_{22}) + (1 - 2\alpha_2) \Sigma_{33} \quad (6.3)$$

which is a generalization of the definition in equation (3.25). The main difference between equations (6.1) and (3.39) appears in the square term, where we now use the square of the Hill norm of the tensor $\boldsymbol{\Sigma}' + \eta \Sigma_h \mathbf{X}$. Recall that the Hill norm is defined for a tensor \mathbf{T} by

$$T_{eq} \equiv \sqrt{\frac{3}{2} \mathbf{T} : \mathbf{h} : \mathbf{T}} \quad (6.4)$$

In the case of axisymmetric loadings about the void axis, equation (6.1) specializes to

$$\frac{h}{h^*} \frac{C}{\sigma_1^2} (\Sigma_{33} - \Sigma_{11} + \eta \Sigma_h)^2 + 2(g+1)(g+f) \cosh \kappa \frac{\Sigma_h}{\sigma_1} - (g+1)^2 - (g+f)^2 = 0 \quad (6.5)$$

where $h^* \equiv 6/(h_{11} + h_{22} + 4h_{33} - 4h_{23} - 4h_{31} + 2h_{12})$. However, as discussed in section C.5 of chapter III, one can show using the definitions of the anisotropy parameters in terms of the strain ratios of the material that the value of h^* is very close to h . Indeed, if one of the material orthotropy directions coincides with the void axis, and the anisotropy parameters are normalized such that h^* is necessarily equal to unity, as is done in the material data reported in Table A of Appendix A, we see that the value of h is close to unity for all the materials in Table A. Hence, we may conclude that the criterion of equation (6.5) is very close to that of equation (3.39). One may also note that the criterion of equation (6.1), unlike (3.39), reduces exactly to the criterion established by Benzerga and Besson [22] for the case of spherical cavities in an anisotropic matrix.

Elasticity may be incorporated by adding to the plastic strain-rate, \mathbf{D}^p , obtained from the normality flow rule of equation (5.1), a hypoelastic strain rate, \mathbf{D}^e , rate obtained from an objective derivative of the stress. The evolution law of porosity is given by equation (5.5), which derives from macroscopic normality and plastic incompressibility of the matrix. For the evolution of void shape parameter, we formally

adopt the proposal of Gologanu et al. [25], given by

$$\dot{S} = \frac{3}{2}sD_{33}^p + 3\left(\frac{1-3\alpha_1}{f} + 3\alpha_2 - 1\right)D_m^p \quad (6.6)$$

where the heuristic factor, s , is given by equation (5.15).

Finally, we also need an equation for the rotation of the void axis during deformation, of the form

$$\dot{\mathbf{e}}_3 = \mathbf{\Omega} \cdot \mathbf{e}_3 \quad (6.7)$$

where $\mathbf{\Omega}$ is the spin tensor. As in [25], we adopt the simplest proposal that the void rotates with the material, in which case $\mathbf{\Omega}$ will be the same as the rotation rate of the material. One may note here that more sophisticated approaches are possible using a spin concentration tensor for the void, as in the works of Kailasam et al. [43].

B. Conclusions

In conclusion, we present the salient features of the new constitutive model developed, which may be considered as the main outputs of this thesis.

- A closed form analytical yield criterion was derived for an anisotropic porous material containing spheroidal voids, using a Hill-Mandel homogenization and approximate limit analysis of a porous RVE, undergoing axisymmetric plastic deformation. The analytical form of the yield criterion, generalized to arbitrary states of loading, is given by equation (6.1).
- A numerical method was developed for determination of upper-bound yield loci for specific anisotropic materials, using the approach detailed in chapter IV. The analytical yield loci were seen to be in close agreement with the numerical data for a wide range of values of the porosity. In particular, the new criterion

was shown to be significantly more accurate than previous analytical criteria proposed by Monchiet et al. [3] for anisotropic materials.

- Analytical expressions for the evolution of the internal microstructural variables, f and S , were developed in chapter V. The model results were validated by comparison to numerical data obtained through the numerical limit analysis approach, as well as direct finite element simulation of anisotropic porous RVEs. The model results were shown to be in reasonable agreement with the numerical data. Particularly, the model was seen to capture the correct trends for the influence of material anisotropy on void shape evolution.

C. Future Work

The main interest in developing sophisticated constitutive models is in the field of ductile fracture modeling. The prediction of fracture modes and the transition between them, during material processing and in service, continues to be a challenge, due to the limitations of analytical models in representing the actual microstructure. Accurate prediction of the evolution of damage parameters like porosity and void shape could lead to improved predictive capability in the simulation of ductile fracture. For Ti alloys, this could lead to improved predictions for the forming limits and optimal loading paths during processing, that minimizes damage growth in the form of porosity. One major challenge is the prediction of specific loading paths that achieve “cavity sealing”, i.e. closure of cracks and voids already present in the material, as a result of the forming process. It is hoped that once the new model is implemented in a finite element code, the results show better agreement with experimentally observed data for damage evolution during processing.

REFERENCES

- [1] A. A. Benzerga, Rupture ductile des tôles anisotropes, Ph.D. thesis, Ecole Nationale Supérieure des Mines de Paris (2000).
- [2] S. Semiatin, V. Seetharaman, I. Weiss, Hot workability of titanium and titanium aluminide alloys-an overview, *Materials Science and Engineering A* 243 (1998) 1.
- [3] V. Monchiet, C. Gruescu, E. Charkaluk, D. Kondo, Approximate yield criteria for anisotropic metals with prolate or oblate voids, *C.R.Mecanique* 334 (2006) 431.
- [4] M. Donachie, *TITANIUM: A Technical Guide*, ASM International, Metals Park, OH, 1988.
- [5] P. Nicolaou, S. Semiatin, The effect of strain-path reversal on cavitation during hot torsion of Ti-6Al-4V, *Metallurgical and Materials Transactions A* 37 (2006) 3697.
- [6] S. Semiatin, G. Lahoti, Deformation and unstable flow in hot forging of Ti-6Al-2Sn-4Zr-2Mo-0.1Si, *Metallurgical and Materials Transactions A* 12 (1981) 1705.
- [7] V. Seetharaman, L. Boothe, C. Lombard, in: *Microstructure/Property Relationships in Titanium Aluminides and Alloys*, Kim, Y-W. and Boyer, R.R. (Eds.), TMS, Warrendale, PA, 1991.
- [8] T. Matsumoto, M. Nishigaki, M. Fukuda, T. Nishimura, in: *Titanium: Science and Technology*, Deutsche Gesellschaft Metallkunde, Oberursel, Germany, 1985.

- [9] P. J. E. Forsyth, C. A. Stubbington, Directionality in structure–property relationships: aluminium and titanium alloys, *Met. Tech.* 2 (1975) 158.
- [10] W. M. Garrison, N. R. Moody, Ductile fracture, *J. Phys. Chem. Solids* 48 (1987) 1035.
- [11] R. Dutton, S. Semiatin, The effect of density anisotropy on the yielding and flow behavior of partially consolidated powder compacts, *Metallurgical and Materials Transactions A* 29 (1998) 1471.
- [12] F. A. McClintock, A criterion for ductile fracture by the growth of holes, *J. App. Mech.* 35 (1968) 363.
- [13] J. R. Rice, D. M. Tracey, On the enlargement of voids in triaxial stress fields, *J. Mech. Phys. Solids* 17 (1969) 201.
- [14] A. L. Gurson, Plastic flow and fracture behavior of ductile materials incorporating void nucleation, growth and interaction, Ph.D. thesis, Brown University, Providence (1975).
- [15] A. L. Gurson, Continuum theory of ductile rupture by void nucleation and growth: part I– yield criteria and flow rules for porous ductile media, *J. Eng. Mat. Tech.* 99 (1977) 2.
- [16] P. Ponte Castañeda, M. Zaidman, Constitutive models for porous materials with evolving microstructure, *J. Mech. Phys. Solids* 42 (1994) 1459.
- [17] P. Ponte Castaneda, The effective mechanical properties of nonlinear composites, *J. Mech. Phys. Solids* 39 (1991) 45.
- [18] G. Rousselier, Ductile fracture models and their potential in local approach of fracture, *Nucl. Eng. Design* 105 (1987) 97.

- [19] J.-B. Leblond, G. Perrin, J. Devaux, An improved Gurson–type model for hardenable ductile metals, *Eur. J. Mechs, A/Solids* 14 (1995) 499.
- [20] K.-C. Liao, J. Pan, S. C. Tang, Approximate yield criteria for anisotropic porous ductile sheet metals, *Mechanics of Materials* 26 (1997) 213.
- [21] A. A. Benzerga, J. Besson, A. Pineau, Modèle couplé comportement–endommagement ductile de tôles anisotropes, in: B. Peseux, D. Aubry, J. P. Pelle, M. Touratier (Eds.), *Actes du 3^{ème} Colloque National en Calcul des Structures*, Presses Académiques de l’Ouest, 1997.
- [22] A. A. Benzerga, J. Besson, Plastic potentials for anisotropic porous solids, *Eur. J. Mech.* 20 (2001) 397.
- [23] M. Gologanu, J.-B. Leblond, J. Devaux, Approximate models for ductile metals containing non-spherical voids – case of axisymmetric prolate ellipsoidal cavities, *J. Mech. Phys. Solids* 41 (1993) 1723.
- [24] M. Gologanu, J.-B. Leblond, J. Devaux, Approximate models for ductile metals containing non-spherical voids — case of axisymmetric oblate ellipsoidal cavities, *J. Eng. Mat. Tech.* 116 (1994) 290.
- [25] M. Gologanu, J.-B. Leblond, G. Perrin, J. Devaux, Recent extensions of Gurson’s model for porous ductile metals, in: P. Suquet (Ed.), *Continuum Micromechanics*, Springer–Verlag, New York (1995) 61.
- [26] M. Gologanu, Etude de quelques problèmes de rupture ductile des métaux, Ph.D. thesis, Université Paris 6 (1997).
- [27] M. Garajeu, Contribution à l’étude du comportement non linéaire de milieux poreux avec ou sans renfort, Ph.D. thesis, Université de Marseille (1995).

- [28] V. Monchiet, O. Cazacu, E. Charkaluk, D. Kondo, Macroscopic yield criteria for plastic anisotropic materials containing spheroidal voids, *Int. J. Plasticity*, In press.
- [29] O. Sovik, The effect of non-spherical void-shape on the evolution of ductile damage, in: J. Petit (Ed.), *11th European Conference on Fracture*, Chameleon Press, Poitiers, France, 1995.
- [30] R. Hill, The essential structure of constitutive laws for metal composites and polycrystals, *J. Mech. Phys. Solids* 15 (1967) 79.
- [31] J. Mandel, Contribution théorique à l'étude de l'écroutissement et des lois d'écoulement plastique, in: *11th International Congress on Applied Mechanics*, Springer, Berlin, 1964.
- [32] P. Suquet, Plasticité et homogénéisation, Ph.D. thesis, Université Pierre et Marie Curie – Paris VI (1982).
- [33] P. Suquet, Analyse limite et homogénéisation, *C. R. Acad. Sci. Paris* 296 (1983) 1355.
- [34] R. Hill, A theory of yielding and plastic flow of anisotropic solids, *Proc. Roy. Soc. London A* 193 (1948) 281.
- [35] B. J. Lee, M. E. Mear, Axisymmetric deformation of power-law solids containing a dilute concentration of aligned spheroidal voids, *J. Mech. Phys. Solids* 40 (1992) 1805.
- [36] I. Gradshteyn, I. Ryzhik, *Table of Integrals, Series, and Products*, Academic Press, Inc., New York, 1980.

- [37] P. Gill, W. Murray, M. Wright, Practical Optimization, Academic Press, New York, 1981.
- [38] Y. C. Liu, L. K. Johnson, Hill's plastic strain ratio of sheet metals, *Met. Trans. A* 16A (1985) 1531.
- [39] J. Besson, R. Foerch, Large scale object oriented finite element code design, *Comput. Methods Appl. Mech. Engrg* 142 (1997) 165.
- [40] R. Foerch, J. Besson, G. Cailletaud, P. Pilvin, Polymorphic constitutive equations in finite element codes, *Comput. Methods Appl. Mech. Engrg* 141 (1997) 355.
- [41] M. Ortiz, J. Simo, An analysis of a new class of integration algorithms for elastoplastic constitutive relations, *International Journal for Numerical Methods in Engineering* 23 (1986) 353.
- [42] J. Simo, T. Hughes, *Computational Inelasticity*, Springer, New York, 1998.
- [43] M. Kailasam, P. Ponte Castaneda, A general constitutive theory for linear and nonlinear particulate media with microstructure evolution, *J. Mech. Phys. Solids* 46 (1998) 427.

APPENDIX A

ANISOTROPY DATA FOR ENGINEERING MATERIALS

Material anisotropy data for sheet materials is usually specified in terms of three strain ratios in the rolling direction (L), 90° from the rolling direction in the plane of the sheet (T) and 45° from the rolling direction in the plane of the sheet (LT). These are designated R^L , R^T and R^{LT} respectively. For bulk materials we have two additional strain ratios in the off-plane directions (TS) and (SL), where S represents the thickness direction for sheet metals [22]. Assuming that the coordinate directions 1, 2 and 3 coincides with the L, T and S directions respectively, and the anisotropy factors are normalized such that the Hill equivalent stress in equation (2.5) equals the yield stress in the 3-direction, one can show that the diagonal elements of the Voigt form of the tensor $\hat{\mathbf{h}}$ are given by (see [22])

$$\begin{aligned}\hat{h}_1 &= \frac{3R^T(R^L R^T + 1)}{2(R^L R^T + R^T + 1)}, & \hat{h}_2 &= \frac{3(R^L R^T + 1)}{2R^L(R^L R^T + R^T + 1)} \\ \hat{h}_3 &= \frac{3(R^L R^T + 1)}{2(R^L R^T + R^T + 1)}, & \hat{h}_4 &= \frac{3(R^L R^T + 1)}{(R^L + 1)(2R^{TS} + 1)} \\ \hat{h}_5 &= \frac{3(R^L R^T + 1)}{R^L(R^T + 1)(2R^{SL} + 1)}, & \hat{h}_6 &= \frac{3}{(2R^{LT} + 1)}\end{aligned}\quad (\text{A.1})$$

For the case of transverse isotropy in the plane of the sheet, we have $R^L = 1/R^T = R^{LT} \equiv R$ and $R^{TS} = R^{SL} \equiv Rh$ [22], in which case

$$\begin{aligned}\hat{h}_1 = \hat{h}_2 = \hat{h}_6 &= \frac{3}{2R + 1}, & \hat{h}_3 &= \frac{3R}{2R + 1} \\ \hat{h}_4 = \hat{h}_5 &= \frac{6}{(R + 1)(2Rh + 1)}\end{aligned}\quad (\text{A.2})$$

Assuming that the void axis coincides with the 3-direction, the anisotropy factors h , h_t and h_a are given by

$$h = \frac{\hat{h}_1 + \hat{h}_2 + 4\hat{h}_3}{6}, \quad h_t = \frac{\hat{h}_1 + \hat{h}_2 + 2\hat{h}_6}{4}, \quad h_a = \frac{\hat{h}_4 + \hat{h}_5}{2}\quad (\text{A.3})$$

The below table, reproduced from [1], contains the values of the strain ratios for a range of engineering materials available in the literature. The column t in the table represents the thickness of the sheet in millimeters. Note that many of the available data is for thin sheet metals for which only the in-plane strain ratios are reported. The calculated values of h , h_t and h_a , using (A.3), are also shown.

Table 2. Table of material anisotropy parameters from the literature. Adapted from [1].

Material	t	R^L	R^T	R^S	R^{TS}	R^{SL}	R^{LT}	h	h_t	h_a
7475-T3										
Al. alloy	32	0.9	1/1.4	1.6	5.0	3.5	1.5	1.0150	0.8521	0.3176
7475-T6										
Al. alloy	32	0.9	1/1.1	1.9	5.0	5.8	1.3	1.0034	0.9217	0.2565
7475-T73										
Al. alloy	32	0.8	1/1.1	1.6	3.0	4.7	1.4	1.0088	0.9252	0.3687
H.S.										
Steel	25	0.5	1/0.7	1.7	1.9	0.7	1.2	1.0130	1.1425	1.2395
C-Mn X52										
Steel	10	0.67	1/0.71	1.05	1.45	1.30	0.91	1.0004	1.1627	0.9495
As-received										
Al. alloy	–	0.57	1/0.62	–	–	–	0.90	1.0008	1.2219	–
-W 25%										
Al. alloy	–	0.64	1/0.69	–	–	–	0.80	1.0006	1.2216	–
-W 50%										
Al. alloy	–	0.46	1/0.50	–	–	–	0.78	1.0009	1.3526	–
Annealed										
Al. alloy	–	0.74	1/0.71	–	–	–	1.76	1.0002	0.9444	–
3004-H12										
Al. alloy	1.0	0.44	1/0.90	–	–	–	0.72	1.0571	1.3414	–
2038-T4										
Al. alloy	0.9	0.68	1/0.71	–	–	–	0.65	1.0002	1.2801	–

Material	t	R^L	R^T	R^S	R^{TS}	R^{SL}	R^{LT}	h	h_t	h_a
5052-H32										
Al. alloy	1.3	0.57	1/0.72	–	–	–	0.59	1.0060	1.3521	–
5182-0										
Al. alloy	1.1	0.63	1/0.71	–	–	–	1.01	1.0015	1.1400	–
SPCE Steel										
Deep-draw	–	1.35	1/1.66	–	–	–	1.14	1.0027	0.8354	–
I.F. Steel	0.9	1.60	1/2.27	–	–	–	2.00	1.0063	0.6175	–
H.S. 950X										
Steel	0.8	0.70	1/0.88	–	–	–	1.27	1.0051	1.0128	–
DP 90-T										
Steel	0.8	0.79	1/1.07	–	–	–	0.86	1.0081	1.0881	–
A-30										
Galvanized										
Steel	0.7	1.31	1/1.77	–	–	–	1.31	1.0056	0.7904	–
Grade 304										
Stainless										
Steel	0.8	0.95	1/0.82	–	–	–	1.06	1.0020	1.0252	–
Copper	0.7	0.90	1/0.96	–	–	–	0.94	1.0004	1.0459	–
70:30										
Brass	0.7	0.90	1/0.78	–	–	–	0.97	1.0019	1.0728	–
Titanium										
(C.P. Grade)	1.2	0.92	1/2.34	–	–	–	1.94	1.0550	0.7419	–
Molybdenum	0.7	1.62	1/2.03	–	–	–	1.46	1.0027	0.7094	–
Zircaloy	0.4	3.3	1/4.5	–	–	–	4.4	1.0028	0.3276	–

VITA

Shyam Mohan Keralavarma obtained his Bachelor of Technology degree in mechanical engineering from the College of Engineering, University of Kerala, Trivandrum, India in May 2000. Before joining Texas A&M University in the fall of 2005, he has worked as a programmer analyst at Infosys Technologies, Mysore, India and Tata Consultancy Services, Mumbai, India. Upon completion of his master's work, he intends to pursue a Ph.D. degree to further his research.

His permanent address is:

“Mohanam”, Edagramom,

Karumom Post,

Trivandrum - 695002,

Kerala, INDIA

Phone: 91-471-2493692

email: skeralavarma@tamu.edu